



Comparative evaluation of non-destructive and CT-derived indicators for stiffness assessment of reclaimed Norway spruce timber

Johannes A. J. Huber^{1,2,3} · Tom Svilans⁴ · Maarja Kauniste⁶ · Niels H. Vonk⁷ · Olof Broman¹ · Eero Tuhkanen⁶ · Wendy Wuyts⁵ · Alar Just⁶ · Martin Tamke⁴ · Mette Ramsgaard Thomsen⁴

Received: 13 December 2025 / Accepted: 4 May 2026
© The Author(s) 2026

Abstract

Reliable evaluation of mechanical performance is a central constraint for structural reuse of reclaimed timber. This study provides a controlled comparative assessment of non-destructive indicators for piece-wise characterisation of reclaimed Norway spruce elements intended for reuse as glulam lamellas. Visual assessment, longitudinal dynamic excitation, and CT-derived modelling indicators were evaluated against global and zone-wise flatwise bending tests on 56 reclaimed beams from a single material stream with known species, cross-section, and initial strength class. Dynamic excitation provided the most reliable single predictor of global bending stiffness at specimen level. Visual assessment showed limited discriminatory power for this comparatively homogeneous material. CT-derived indicators based on density and orientation fields reproduced principal intra-member stiffness variations associated with knots and fibre disturbance and showed predictive capability of similar order to established mechanical non-destructive indicators. Systematic differences between methods were primarily attributable to moisture-state uncertainty, modelling assumptions, and the global nature of the mechanical reference tests. Strength-related results, based on a limited destructive subset, are interpreted as exploratory. Within these bounds, the study establishes a comparative reference dataset for multi-modal evaluation of reclaimed structural timber and demonstrates how conventional and volumetric indicators complement each other in resolving global stiffness and intra-member variability relevant to allocation in engineered wood products.

✉ Johannes A. J. Huber
johannes.huber@ltu.se

Tom Svilans
tsvi@kglakademi.dk

Maarja Kauniste
maarja.kauniste@taltech.ee

Niels H. Vonk
niels.vonk@tno.nl

Olof Broman
olof.broman@ltu.se

Eero Tuhkanen
eero.tuhkanen@taltech.ee

Wendy Wuyts
info@omtre.no

Alar Just
alar.just@taltech.ee

Martin Tamke
martin.tamke@kglakademi.dk

Mette Ramsgaard Thomsen
mette.thomsen@kglakademi.dk

- 1 Wood Science and Engineering, Department of Engineering Sciences and Mathematics, Luleå University of Technology, Forskargatan 1, 931 94 Skellefteå, Sweden
- 2 Wood K Plus - Kompetenzzentrum Holz GmbH, Klagenfurter Straße 87–89, 9300 St. Veit an der Glan, Austria
- 3 Materials Science, Department of Engineering Sciences and Mathematics, Luleå University of Technology, Laboratorievägen 14, 971 87 Luleå, Sweden
- 4 Centre for Information Technology and Architecture (CITA), Royal Danish Academy, Philip de Langes Allé 10, 1435 Copenhagen, Denmark
- 5 Omtre AS, Follumveien 100, 3515 Hønefoss, Norway
- 6 Department of Civil Engineering and Architecture, Tallinn University of Technology, Ehitajate tee 5, 19086 Tallinn, Estonia
- 7 TNO - Building Materials and Structures, Molengraaffsingel 8, 2629JD Delft, The Netherlands

1 Introduction

1.1 Reclaimed timber in circular construction

The construction sector faces the dual challenge of expanding infrastructure while reducing greenhouse-gas emissions. Timber can contribute to both goals, particularly when reused from existing building stocks, off-cuts or waste rather than sourced as virgin material. Reuse extends service life, preserves biogenic carbon, and reduces demand for primary resources (Churkina et al. 2020; Nußholz et al. 2023; Howard et al. 2022). Within circular construction strategies, reclaimed timber therefore represents a potentially high-value structural resource rather than a low-grade waste stream (Byers et al. 2024; Grüter et al. 2023).

Cascading use is central to circular timber strategies: material should be directed to the highest-value structural application compatible with its remaining performance (Hudert and Pfeiffer 2019). Recent research and demonstration projects show that reclaimed timber can be integrated into engineered products such as glulam and cross-laminated timber, provided that variability and uncertainty are explicitly managed (Rose et al. 2018; Chúláin et al. 2023; Dong et al. 2024b; Vonk et al. 2024). European initiatives increasingly treat reclaimed structural timber as a secondary resource base for engineered construction systems (Dong et al. 2024a; Pronk et al. 2022; Lebossé et al. 2022; Bergsagel and Heisel 2023; Asa et al. 2024; Kauniste et al. 2024). It is emphasised that reliable reuse depends less on material availability than on the ability to evaluate mechanical performance and assign suitable structural roles (Novais Passarelli et al. 2025; Heisel and Bergsagel 2025; Niederwestberg et al. 2025; Godina et al. 2025).

Despite this potential, structural reuse remains limited by technical and economic barriers (Byers et al. 2024; Thomsen et al. 2023). Timber already exhibits large natural variability, even for known origin, species, and geometry. Reclaimed material amplifies uncertainty through unknown provenance and processing, altered geometry, and heterogeneous exposure and loading histories. Ageing and environmental exposure can introduce damage mechanisms that are difficult to detect by routine inspection, and long-term loading can reduce strength more than stiffness through duration-of-load effects (Crews and Mackenzie 2008; Falk et al. 2008; Cavalli et al. 2016). Embedded fasteners, cavities, and surface treatments add both structural discontinuities and measurement artefacts (Bergsagel and Heisel 2023). As a result, conservative assumptions dominate reuse decisions, and structurally capable material is frequently downgraded or diverted to non-structural applications (Novais Passarelli et al. 2025; Heisel and Bergsagel 2025).

A promising route is to shift from batch-level certification logic to piece-wise allocation into engineered products. In glulam, for example, performance can be influenced by how lamellas are selected and positioned, making stiffness-resolved information valuable for allocating heterogeneous reclaimed stock to stress-appropriate locations (Tamke et al. 2021). Automated matching workflows are being developed (Haakonsen et al. 2024). This motivates assessment approaches that treat reclaimed timber *as received*, with limited prior information, high intra- and inter-piece variability, and the need for reliable and automated decisions at the element scale (Niederwestberg et al. 2025; Godina et al. 2025).

1.2 Non-destructive evaluation of reclaimed timber

A broad range of non-destructive evaluation (NDE) techniques is available for assessing mechanical properties of timber. Visual assessment, dynamic excitation, ultrasonic and stress-wave methods, and local penetration or drilling resistance measurements provide indicators of stiffness, density, and strength (Piazza and Riggio 2008; Rinn et al. 1996; Piazza and Del Senno 2021). For reclaimed material, combinations of methods are often proposed because individual techniques tend to correlate more strongly with stiffness than with strength (Piazza and Del Senno 2021) and may not capture hidden defects or degradation (Novais Passarelli et al. 2025).

Recent literature on reused structural timber highlights the need to integrate mechanical, geometrical, and material information at the element level (Heisel and Bergsagel 2025; Niederwestberg et al. 2025). Existing studies demonstrate feasibility, but reported predictive performance varies widely with material stream, species, and reference testing, and comparative benchmarks across measurement modalities remain limited (Ranttila et al. 2025; Godina et al. 2025).

X-ray computed tomography (CT) provides detailed volumetric information on internal density, from which wood physical properties (Lindgren 1992; Hansson et al. 2017), anatomical features (Longuetaud et al. 2012), and fibre orientation (Hu et al. 2022, 2025) can be inferred. CT is used industrially to optimise sawing (Rais et al. 2017) and has been employed in research to derive predictors and computational models of stiffness and strength of virgin timber (Huber et al. 2022), complementing models derived from surface data (Lukacevic et al. 2019). Although CT is not currently practical for routine assessment of reclaimed timber, it offers a high-resolution reference modality against which more scalable sensing and modelling approaches can be evaluated. The literature emphasises the role of reuse workflows of such reference datasets in developing reliable,

automated assessment pipelines (Novais Passarelli et al. 2025).

1.3 Performance assessment

In timber design, stiffness, strength, and density are the central properties. While strength dominates assessment efforts, stiffness and density are often governing due to serviceability limits and are more directly accessible to repeated non-destructive measurement. For virgin sawn timber, these properties are usually determined through strength grading, where non-destructively measured *indicating properties* (IPs), e.g. resonance frequency, density, slope of grain, or knot characteristics, are related to *grade-determining properties* (strength, stiffness, density) through calibration (Ridley-Ellis et al. 2016). The outcome is assignment to a strength class defined by characteristic strength and density and mean stiffness (EN 338 2016).

Conventional grading relies on homogeneous, well-documented populations and extensive destructive calibration, which is difficult to reconcile with heterogeneous reclaimed stock and incomplete documentation (Novais Passarelli et al. 2025; Niederwestberg et al. 2025). Existing standards for reused timber, such as NS 3691 and UNI 11119, provide guidance for inspection and visual classification but remain limited in predictive scope and calibration for broader use (UNI 11119 2004; Piazza and Riggio 2008; Piazza and Del Senno 2021; Kauniste et al. 2024).

Consequently, recent work increasingly treats reclaimed timber assessment as element-wise performance evaluation rather than direct transfer of strength-class logic. Many studies address highly heterogeneous material streams spanning multiple species, geometries, and provenance histories (Ranttila et al. 2025; Godina et al. 2025). While this reflects practical reuse scenarios, such heterogeneity can obscure the relative performance of different assessment modalities

because variability arising from species, dimensions, and prior grading is superimposed on usage-related effects.

A complementary approach is to examine reclaimed timber from a controlled material stream with known species, cross-section, and initial grading, but exhibiting typical use-related alterations such as fastener holes, local damage, and storage effects. In this setting, differences between assessment methods can be evaluated with reduced confounding from growth-related or geometric variability, enabling a clearer comparison of how different indicators derived from various measurement modalities or models relate to experimentally observed mechanical behaviour at member and sub-member scale. Such controlled comparative benchmarks remain scarce in the literature but are needed to establish reference cases for subsequent studies on more heterogeneous reclaimed material.

1.4 Objective

This study provides an experimental comparative assessment of non-destructive indicators for piece-wise evaluation of reclaimed Norway spruce timber from a single, controlled material stream intended for reuse as glulam lamellas. The examined elements share species, cross-section, and original strength class but exhibit typical use-related features such as fastener holes, edge damage, and storage-induced variability.

Visual assessment, dynamic excitation, and CT-derived modelling indicators are examined against global and zone-wise bending tests. The focus lies on two questions: (i) how CT-derived structural descriptors compare with established non-destructive indicators in predicting stiffness and strength-related behaviour, and (ii) how reliably these methods capture intra-member variability relevant to lamella-level allocation.

By analysing a comparatively homogeneous reclaimed sample, the study isolates usage- and defect-related variability and establishes a reference workflow for multi-modal assessment. The aim is to quantify the comparative utility and limitations of the applied methods for piece-wise and intra-piece evaluation and allocation of reclaimed timber.

2 Materials and methods

2.1 Specimens and experimental programme

The study material comprised 56 reclaimed Norway spruce (*Picea abies*) construction timber elements (Fig. 1). The elements originated from a student-housing construction site in Kringsjø (Norway), where they had been used temporarily and subsequently discarded. The material exhibited typical



Fig. 1 Labelled reclaimed timber specimens

signs of prior handling and use, including fastener holes, local crushing at ends, and irregular cavities from nail and screw removal. After collection, the timber was stored under sheltered outdoor conditions at Omtre (Hønefoss, Norway) for approximately two years prior to testing.

The specimens had nominal cross-sectional dimensions of $49 \times 98 \text{ mm}^2$ and lengths between 1904 mm and 2862 mm. All pieces were originally machine graded as C24 (EN 338 2016), as indicated by surface markings. The dataset therefore represents a comparatively homogeneous reclaimed stock with known species, geometry, and initial grading, but with visible signs of prior use and handling.

Each specimen underwent X-ray computed tomography (CT) scanning at Luleå University of Technology (LTU, Sweden), followed by dynamic excitation measurements, visual grading, and flatwise bending tests at Tallinn University of Technology (Taltech, Estonia). This sequence enabled direct comparison of indicators derived from imaging, mechanical response, and visual inspection against experimentally measured stiffness and, for a subset, bending strength. In addition, zone-wise bending tests were conducted to characterise intra-specimen variability and to provide local reference values for comparison with spatially resolved indicators.

The specimens experienced three distinct moisture states across the measurement sequence: (i) during CT scanning after short-term winter storage in Skellefteå (no direct MC measurement), (ii) upon arrival to the laboratory in Tallinn after transport under uncertain weather exposure (MC estimated for dynamic excitation by capacitive measurements on longitudinal faces), and (iii) after several weeks of acclimatisation in the Tallinn laboratory (MC measured gravimetrically for a subset of 28 specimens using oven-dry cut-offs after bending tests). Gravimetric MC was not obtained for all specimens because the material was reserved for subsequent glulam production. These differing moisture states between measurement stages represent a systematic source of offset between methods rather than intrinsic material variability.

2.2 Evaluated quantities and indicators

The comparison focuses on indicators related to stiffness, density, and bending strength, as these quantities govern structural performance and are commonly used in both conventional grading and reuse assessment. Rather than treating them as intrinsic material constants, they are considered here as measurable or inferable quantities that depend on local material state, moisture conditions, and defect distribution.

All methods examined in this study provide either direct measurements or derived indicators of these quantities at

different spatial resolutions. Dynamic excitation and visual grading yield specimen-level predictors; CT-based models provide spatially resolved density- and stiffness-related indicators; and flatwise bending tests provide experimental reference values at both global and intra-specimen zone level. Strength values are available only for a subset of specimens and are therefore treated as supplementary reference data. For comparability across methods, quantities are expressed at a reference moisture content of 12% where applicable.

2.3 CT scanning

X-ray CT was used as a high-resolution reference measurement to obtain volumetric density and geometry fields for each specimen. The CT data serve as a benchmark for deriving spatially resolved indicators and for comparing model-based predictions with established non-destructive measurements.

Scanning was performed using a sawmill CT system (Microtec Mito) adapted for research use. Prior to scanning, the specimens were stored under sheltered outdoor conditions for approximately two weeks, during which ambient temperature and relative humidity were recorded. All elements were scanned in batches of four and positioned with the wide face vertical to ensure consistent orientation relative to growth direction and geometry (Fig. 2a). Each specimen was labelled to maintain traceability between physical samples and reconstructed volumes.

The scanner used a helical cone-beam acquisition at 180 kV tube voltage and 5.55 mA current. Tomographic reconstruction used a proprietary implementation of the Katsevich algorithm (Katsevich 2004) and produced voxel volumes with $0.5 \times 0.5 \times 0.5 \text{ mm}^3$ resolution. The resulting 16-bit greyscale intensities $\mathcal{I}(x, y, z)$ were converted using machine-specific calibration to density fields $\rho_{CT}(x, y, z)$ in kg/m^3 , forming the basis for subsequent modelling and indicator derivation.

2.4 CT-based models

The greyscale voxel field $\mathcal{I}(x)$ reflects local density and contains sufficient anatomical contrast for reconstructing fibre orientation and assigning spatially varying orthotropic stiffness. Building on previous frameworks (Huber et al. 2022, 2023), this study derives geometric, anatomical, and mechanical fields directly from intensities and local gradients in the CT data, without explicit segmentation of knots or pith. All resulting fields are aggregated in a unified data structure, called *Body of Properties* (BoP), and subsequently evaluated through two modelling approaches: a 3D finite-element (FE) model and a meshless continuum model (CM), see Fig. 3.

Fig. 2 CT scanning of reclaimed timber: **a** positioning in the scanner, and **b** a representative single-slice CT image of a scanned batch

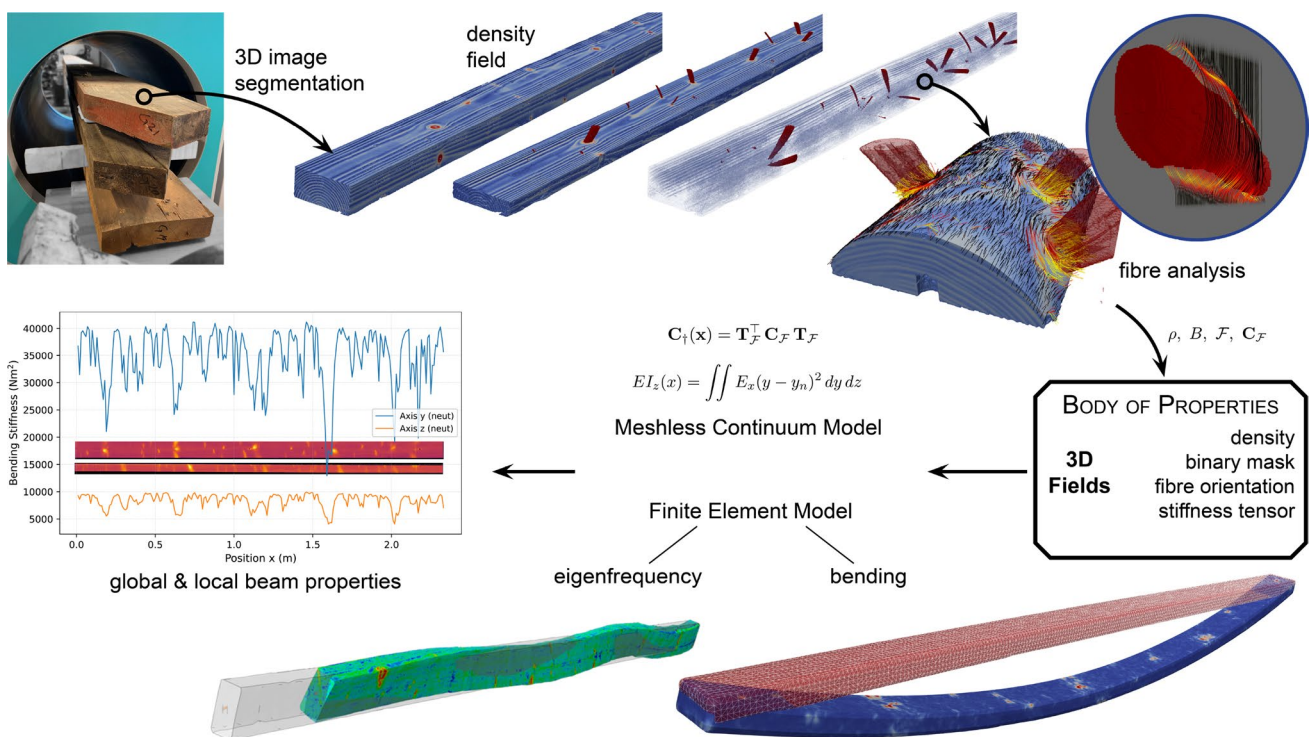
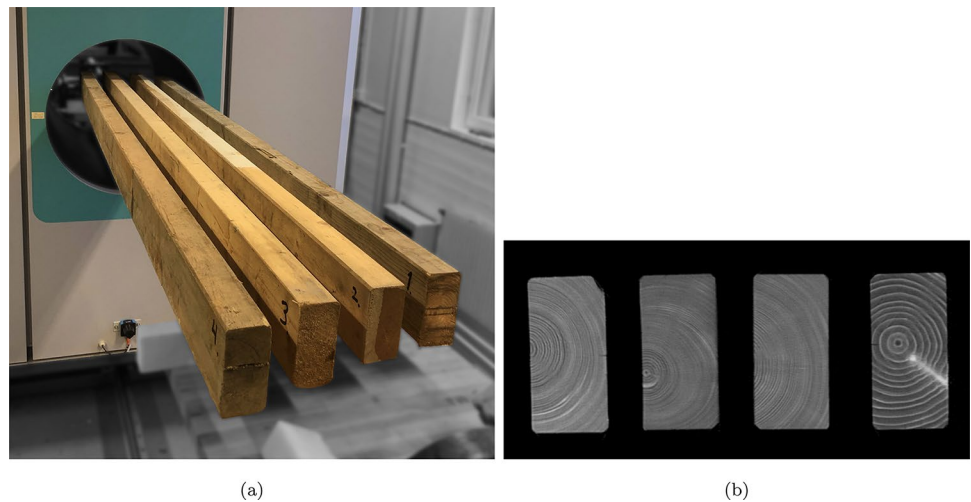


Fig. 3 Overview of the CT-based analysis pipeline, showing preprocessing, material field reconstruction, generation of the Body of Properties, and subsequent model evaluations

Spatial position is denoted by the coordinate vector $x = (x, y, z)^T$, where x is the longitudinal axis of the specimen, y the strong-axis direction, and z the weak-axis direction of the global specimen coordinate system (Fig. 4).

2.4.1 CT data preprocessing and segmentation

All CT data processing was performed using custom Python scripts based on the `pydip` interface to `DIPimage` (Luengo and Contributors 2025). For each slice, wood tissue was segmented from air using the intra-mode minimum

of the greyscale histogram in the range $50\text{--}350 \text{ kg/m}^3$ (Prewitt and Mendelsohn 1966). A preliminary thresholding step separated individual specimens within each batch through connected-component analysis. For each isolated specimen, remaining small cavities were removed with 3D hole filling, followed by one dilation–erosion cycle to ensure a topologically consistent binary wood mask $B(x)$.

Specimens were not perfectly aligned in the scanner. The principal axes of $B(x)$ were therefore obtained from second-order central image moments (Hu 1962) and used to rotate each volume such that its longitudinal axis aligned

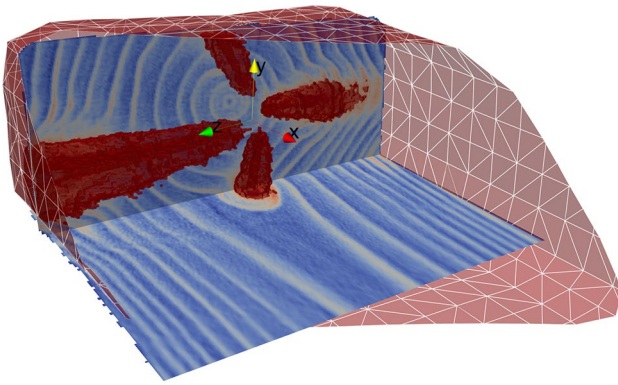


Fig. 4 Global specimen coordinate system used throughout the CT-based modelling. The longitudinal axis defines x ; the strong- and weak-axis bending directions define y and z , respectively

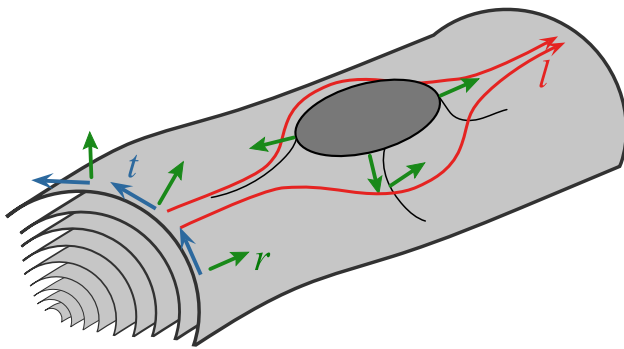


Fig. 5 Density isosurfaces representing earlywood–latewood layering. Local density gradient orientations align with the radial (r) direction, while the longitudinal (l) and tangential (t) directions follow from the principal continuity direction and its orthogonal complement

with the global x -direction. The aligned mask served as the basis for geometry extraction, BoP generation, and sampling in all subsequent analyses.

2.4.2 Fibre orientation reconstruction

In softwoods with visible growth rings, the alternating earlywood–latewood layers form density variations that appear as quasi-isosurfaces in the CT volume. Their local normals indicate the radial direction, corresponding to the direction of steepest density change (Huber 2021; Hu et al. 2025). This anatomical structure provides reliable input for gradient-based orientation analysis and motivates the use of the 3D Gradient Structure Tensor (GST) (Bigun et al. 2004; Krause et al. 2010; Huber et al. 2023) to obtain a continuous material coordinate system (Fig. 5).

Let $\mathcal{I}_\sigma(x)$ denote the density field smoothed with a Gaussian kernel of standard deviation σ . The GST is defined as

$$J(x) = g_\omega * (\nabla \mathcal{I}_\sigma(x) \nabla \mathcal{I}_\sigma(x)^\top), \quad (1)$$

where g_ω is a Gaussian kernel with scale ω providing spatial regularisation, $*$ denotes convolution and ∇ is the gradient operator.

$J(x)$ is a positive semi-definite 3×3 symmetric matrix that characterises the local distribution of gradient orientations in the image. Its eigendecomposition

$$J v_i = \lambda_i v_i, \quad \lambda_1 \geq \lambda_2 \geq \lambda_3, \quad (2)$$

yields three orthonormal eigenvectors v_i . In regions where the eigenvalues are well separated, v_1 corresponds to the direction of steepest density increase and was used as the *radial* material direction. The direction of highest continuity, v_3 , was used to approximate the *longitudinal* material direction, i.e. the fibre orientation. The *tangential* direction followed from the cross product of these two vectors. This produced a continuous orthotropic material coordinate system $\mathcal{F}(x)$ at voxel resolution, including in knot-affected regions, without requiring explicit knot segmentation.

2.4.3 Stiffness tensor assignment

A spatially varying orthotropic stiffness tensor $C_{\mathcal{F}}$, aligned with $\mathcal{F}(x)$, was assigned following \mathcal{L}_1 from Huber et al. (2022):

$$C_{\mathcal{F}}(x) = \left(\frac{\rho_{CT}(x)}{\rho_0} \right)^2 \varkappa(x) C_0 \quad (3)$$

where ρ_0 and C_0 are the reference density and stiffness tensor for Norway spruce at 12% MC (Dinwoodie 2000). To account for the different mechanical character of knots, a penalisation factor $\varkappa = 0.5$ was applied where $\rho_{CT} > 900 \text{ kg/m}^3$, and $\varkappa = 1$ otherwise (Lukacevic et al. 2019).

2.4.4 Body of properties

The fields $\rho_{CT}(x)$, $B(x)$, $\mathcal{F}(x)$ and $C_{\mathcal{F}}(x)$ were integrated into the BoP, a single volumetric data structure using OpenVDB grids (Museth 2013; Svilans et al. 2022). This enabled consistent data exchange with simulations, efficient sampling along arbitrary beam sections, and a compact storage format. All subsequent FE and CM computations queried material values via the BoP.

2.4.5 3D finite element model

Geometry was extracted from $B(x)$ using marching cubes (Lorenson and Cline 1987), converted to a triangular surface mesh and decimated using Open3D (Zhou et al. 2018) to a 10 mm surface resolution. A quadratic tetrahedral mesh

(largest size 7.5 mm) was generated in Gmsh (Geuzaine and Remacle 2009). FE analyses (static bending and eigenfrequency) were conducted in CalculiX (Dhondt 2004). For each element, the local $C_{\mathcal{F}}$ and \mathcal{F} were retrieved from the BoP using a custom UMAT subroutine. Element density was set to the specimen-level mean ρ_{CT} .

For the bending analysis, nodes were embedded along the specimen centreline at 10 mm spacing, to query deflections. A simply supported pure bending configuration was imposed. End sections were kinematically coupled to end nodes. One end node was fixed in translation, the other allowed translation only along x . Rotations were locked except about y and opposite moments M were applied at the end nodes. The mid-span deflection $w_{FE,mid}$ and the deflection profile $w_{FE}(x)$ were extracted at the centreline.

The apparent global stiffness from midpoint bending was computed as

$$E_{FE,w} = \frac{ML^2}{8 I_z w_{FE,mid}}, \tag{4}$$

with second moment of area I_z from nominal specimen dimensions. A local curvature-based stiffness profile $E_{FE,\kappa}(x)$ was derived by assuming an inhomogeneous Euler–Bernoulli beam under constant moment M :

$$EI_z(x) \kappa(x) = M, \tag{5}$$

where $EI_z(x)$ and $\kappa(x)$ are the locally varying bending stiffness and curvature, respectively. Since $\kappa \approx d^2w/dx^2$,

$$EI_z(x) = M \left(\frac{d^2w(x)}{dx^2} \right)^{-1}, \quad E_{FE,\kappa}(x) = \frac{EI_z(x)}{I_z}, \tag{6}$$

where $w_{FE}(x)$ was used for deflections and the second derivative was obtained via a Savitzky-Golay filter (Savitzky and Golay 1964).

In the eigenfrequency analysis, the first 20 frequencies were computed and the lowest longitudinal mode was used for $f_{0,FE}$. A dynamic stiffness $E_{FE,dyn}$ was calculated as

$$E_{FE,dyn} = (2L f_{0,FE})^2 \rho_{CT}. \tag{7}$$

2.4.6 Meshless continuum model

This model performs direct cross section-wise continuum mechanical evaluations of the BoP on a regular grid, combined with Euler–Bernoulli beam theory, to obtain stiffness profiles along the specimen length (Huber 2021; Huber et al. 2022). A structured grid with $1 \times 1 \text{ mm}^2$ cross-sectional

resolution and 10 mm spacing along x was used which linearly interpolated the BoP fields at each grid point.

At each point, $C_{\mathcal{F}}$ was rotated to global coordinates:

$$C_{\dagger}(x) = T_{\mathcal{F}}^{\top} C_{\mathcal{F}} T_{\mathcal{F}}, \tag{8}$$

where $C_{\dagger}(x)$ is the rotated tensor and $T_{\mathcal{F}}$ the corresponding 6×6 transformation matrix (Ormarsson 1999; Huber et al. 2022). The compliance tensor $S = C_{\dagger}^{-1}$ gave the uniaxial and shear stiffness components:

$$E_x = \frac{1}{S_{11}}, \quad G_{xy} = \frac{1}{S_{44}}. \tag{9}$$

For each cross section, the neutral axis y_n , the bending stiffness $EI_z(x)$ around the neutral axis, the axial stiffness $EA(x)$ and the shear stiffness $GA_y(x)$ were computed integrating over $B(x)$ (Huber 2021):

$$y_n = \frac{\iint E_x y \, dy \, dz}{\iint E_x \, dy \, dz}, \tag{10}$$

$$EI_z(x) = \iint E_x (y - y_n)^2 \, dy \, dz, \tag{11}$$

$$EA(x) = \iint E_x \, dy \, dz, \tag{12}$$

$$GA_y(x) = \iint G_{xy} \, dy \, dz, \tag{13}$$

Corresponding sectional geometric quantities $A(x)$, $I_z(x)$ and mean density were evaluated analogously.

Section-equivalent stiffness profiles $E_{CM,EI}(x)$, $E_{CM,EA}(x)$, and $G_{y,CM,GA}(x)$, based on bending, axial, and shear stiffness, respectively, were then obtained:

$$E_{CM,EI}(x) = \frac{EI_z(x)}{I_z(x)}, \quad E_{CM,EA}(x) = \frac{EA(x)}{A(x)}, \tag{14}$$

$$G_{CM,GA}(x) = \frac{GA_y(x)}{A(x)}.$$

2.4.7 Model-based predictors

Predictors for regression models were derived from both modelling approaches, at the *global* specimen level and at *zone* level (aligned with the mechanical test zones, see Sect. 2.7). The scalar quantities were used directly as global predictors, while for spatially varying quantities, arithmetic means over the respective regions yielded global and

zone-level predictors. A summary for the predictor variables is provided in Table 1.

2.5 Visual assessment

Assessment based on grading rules was performed only on the specimens selected for destructive bending tests and was carried out at the specific longitudinal zone used in the destructive testing (Sect. 2.7). This ensured that the visual classification corresponded to the material volume governing the tested bending response. Since only one zone per evaluated specimen was assessed, the resulting category was also used as the specimen-level visual indicator.

All faces were inspected under uniform lighting. Knots, slope of grain, cracks, wane, distortions, decay, and other surface irregularities were recorded and measured manually (ruler and caliper) and documented photographically. Feature measurement followed EN 1309-3 (EN 1309-3 2018), while categorisation was performed by applying three regional rule sets: SS 230120 (2010), NS 3691-3 (2025), and UNI 11119 (2004). INSTA 142 is aligned with EN 1912 (2024) and EN 14081-1 (2019) and assigns grades T0–T3 with indicative mapping to strength classes C14–C30 through EN 338 (2016). NS 3691-3 extends visual rules to reclaimed timber by adding criteria for contamination, end-grain integrity, and indicators consistent with ageing or prior loading. UNI 11119, with lowest class III and highest I, was included because it is widely used for historic timber and is frequently cited in the reclaimed-timber literature; in view of reported limitations in category assignment reliability, it is treated here as a comparative reference rather than a benchmark.

All assessments were performed by trained personnel. Ambiguous cases were checked by a second individual, and disagreements were resolved by consensus. For comparison with experimental bending strength, each rule set was mapped to the corresponding characteristic bending strength

Table 1 Model-derived predictors from CT-based modelling

Source	Global	Zone
$E_{FE,w}$	$E_{FE,w}$	–
$f_{0,FE}$	$f_{0,FE}$	–
$E_{FE,dyn}$	$E_{FE,dyn}$	–
$E_{FE,\kappa}(x)$	$E_{FE,\kappa}$	$E_{FE,\kappa,i}$
$E_{CM,EA}(x)$	$E_{CM,EA}$	$E_{CM,EA,i}$
$E_{CM,EI}(x)$	$E_{CM,EI}$	$E_{CM,EI,i}$
$G_{y,CM,GA}(x)$	$G_{y,CM,GA}$	$G_{y,CM,GA,i}$
$\rho_{CT}(x)$	ρ_{CT}	$\rho_{CT,i}$

Global values represent arithmetic means over the full specimen length; zone values represent arithmetic means over the mechanically tested zones

stated in the respective document, yielding $\sigma_{f,vis,INS}$, $\sigma_{f,vis,NS}$, and $\sigma_{f,vis,UNI}$.

2.6 Dynamic excitation

Longitudinal dynamic excitation was applied to estimate the stiffness and strength of each specimen using a hand-held mobile timber grader (*MTG 960, Brookhuis*, the Netherlands). The method determines a dynamic modulus of elasticity, $E_{DE,dyn}$, as an IP, which serves as input to regression models predicting the grade-determining properties: static modulus of elasticity E_{DE} and bending strength $\sigma_{f,DE}$, following EN 14081 (2018).

Each specimen was excited longitudinally by an internal impactor, and the vibration response was recorded by an integrated accelerometer. From the frequency spectrum (resolution 4 Hz), the fundamental frequency f_0 was identified. For specimens with intact ends, four impacts (two per end) were performed, and the average f_0 was used for subsequent analysis. Density during the measurement (ρ_{DE}) was determined gravimetrically using nominal dimensions, while MC was determined from repeated measurements at both specimen ends (longitudinal faces) using a handheld capacitive meter (*FMW-T, Brookhuis*, the Netherlands). The correction of ρ_{DE} to the 12% MC reference state ($\rho_{12,DE}$) followed EN 384 (2016):

$$a_{MC,DE} = \frac{MC_{DE} - 12}{100}, \quad \rho_{12,DE} = \rho_{DE} \left(1 + \frac{a_{MC,DE}}{2} \right) \quad (15)$$

where MC is in percent.

The dynamic predictor of the MTG is computed as:

$$E_{DE,dyn} = (2L f_0 c_{MTG})^2 \rho_{12,DE} \quad (16)$$

where L is the specimen length in mm, c_{MTG} a dimensionless correction factor, f_0 is in Hz, and ρ_{12} in kg/m³. The details of the internal computation, including c_{MTG} , are proprietary to *Brookhuis*, though similar formulations have been published (Ravenshorst and Van De Kuilen 2013; Moltini et al. 2022).

The MTG software uses regression to infer E_{DE} and $\sigma_{f,DE}$ from $E_{DE,dyn}$. For this study, strength categories were defined with a bin width of one to allow continuous, specimen-wise estimation, in contrast to the broader grading classes defined in EN 338 (2016).

2.7 Zone-wise flat-wise bending test

Four-point bending tests were conducted in accordance with EN 408 (2012) to obtain reference stiffness and, for a subset, bending strength. Tests were performed in flatwise

orientation (bending about the weak axis). This configuration was selected for two reasons. First, the reclaimed elements were intended for subsequent use as lamellas in engineered wood products, where flatwise behaviour is structurally relevant. Second, the flatwise configuration permits shorter test spans relative to specimen length, enabling multiple measurement zones along each element and thereby supporting the study objective of comparing piecewise indicators and intra-specimen variability.

It is noted that structural timber in service is commonly loaded edgewise and that strength classes according to EN 338 refer to edgewise bending tests. Differences between flatwise and edgewise properties may arise due to anisotropy, knot distribution through the cross section, and shear effects. The present results should therefore be interpreted primarily in a comparative sense for indicator evaluation and lamella-level assessment rather than as a direct basis for conventional strength-class assignment.

All tests were carried out on a universal testing machine (*walter+bai LFM Series*) with a 600 kN load cell. Each specimen was tested non-destructively in two or three longitudinal zones, depending on length, located near the start (x_1), midspan (x_2), and end (x_3), see Fig. 6. Each zone was loaded within the elastic range to determine a zone-wise modulus of elasticity $E_{FB,i}$. This repeated elastic loading provides a mechanically based indicator analogous to proof-loading approaches used in industrial grading contexts.

Following the non-destructive tests, 15 specimens were selected and loaded to failure in one previously tested zone (random selection) to obtain flatwise bending strength $\sigma_{f,FB}$. The remaining specimens were preserved for subsequent allocation to glulam production.

The support span L_i and loading-point distance a were both 270 mm, and the loading rate was 0.15 mm/s. Midspan deflection was measured with an LVDT (5 μ m resolution). MC at testing, MC_{FB} , was determined gravimetrically for 28 specimens (including all destructively tested specimens) using cut-offs taken after testing to preserve material for subsequent glulam manufacture.

A malfunction in the instrumentation intended to measure differential deflection within the pure bending region prevented determination of local modulus of elasticity in that region. Consequently, zone-wise moduli represent

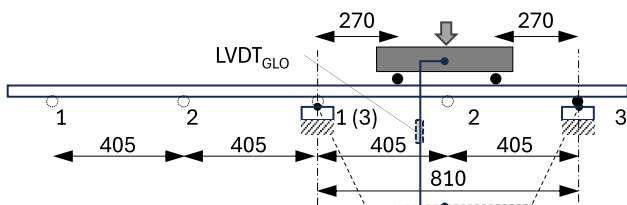


Fig. 6 Zone-wise four-point bending configuration

global bending stiffness over the test span and include shear contributions.

Zone-wise (global) modulus of elasticity was calculated from the linear portion of the load–deflection curve according to EN 408:

$$E_{FB,i} = \frac{3a L_i^2 - 4a^3}{2b_i h_i^3 \left(2 \frac{\Delta w_i}{\Delta F_i} - \frac{6a}{5G b_i h_i} \right)} \text{ for } i = 1, 2, 3 \quad (17)$$

where L_i and a are in mm, b_i and h_i denote cross-sectional dimensions in mm, ΔF_i is the applied load increment in N, and Δw_i the corresponding midspan deflection increment in mm. The shear modulus $G = 650$ MPa was assumed following EN 408. A shear-free modulus $E_{FB,G,\infty,i}$ was additionally computed by setting $G \rightarrow \infty$ to quantify sensitivity to the shear assumption. For specimen-level comparisons, zone-wise values were averaged.

For specimens tested to failure, bending strength $\sigma_{f,FB}$ was calculated as:

$$\sigma_{f,FB} = \frac{3F_{f,i} L_i}{2b_i h_i^2}, \quad (18)$$

where $F_{f,i}$ is the maximum load in N at failure. As only one zone per specimen was tested to failure, strength values are reported at specimen level.

Adjustments to reference MC and size followed EN 384 (2016):

$$\sigma_{f,FB,adj} = \sigma_{f,FB} (1 + 0.02 a_{MC,FB}), \quad (19)$$

$$a_{MC,FB} = (MC_{FB} - 12) / 100,$$

$$E_{FB,adj,i} = 1.3 E_{FB,i} (1 + a_{MC,FB}) - 2690 \text{ MPa}. \quad (20)$$

2.8 Comparisons

All measured quantities and derived variables used are summarised in Table 2. Predictive performance was evaluated using linear regression between each predictor and the experimentally measured target variables. Model performance is reported using the coefficient of determination (R^2), root-mean-square error (RMSE), mean absolute error (MAE), and Pearson’s correlation coefficient (r). For visual grading, which yields ordinal data, associations with experimental properties were quantified using Spearman’s rank correlation coefficient (r_s).

For bending strength, the number of destructively tested specimens was limited and strength-related comparisons are therefore treated as exploratory and evaluated separately. A leave-one-out cross-validation (LOO) procedure

Table 2 Overview of all measurement modalities with measured quantities and derived variables

Method	Measured quantities	Derived variables
CT-based models	$\rho_{CT}(x), B(x), \mathcal{F}(x)$	$\rho_{CT}(x)$: sectional mean density, $E_{FE,w}$: mid-point based bending stiffness, $E_{FE,\kappa}(x)$: curvature-based stiffness profile, $E_{FE,dyn}$: dynamic stiffness from eigenfrequency, $E_{CM,EI}(x), E_{CM,EA}(x), G_{CM,GA}(x)$: sectional stiffness profiles (bending, axial, shear)
Dynamic excitation	$f_0, \rho_{12,DE}, MC_{DE}$	E_{DE} : static bending stiffness, $\sigma_{f,DE}$: bending strength
Visual grading	INSTA 142, NS 3691-3, UNI 11119	$\sigma_{f,vis,INS}, \sigma_{f,vis,NS}, \sigma_{f,vis,UNI}$: visual equivalent strength estimates
Bending tests	dimensions b_i, h_i , Load–deflection curves, $F_{f,i}$ (subset), MC_{FB} (subset)	$E_{FB,G}$: global bending stiffness, $E_{FB,G,adj}$: adjusted global bending stiffness (subset), $E_{FB,G,\infty}$: shear-free global bending stiffness, $\sigma_{f,FB}$: adjusted bending strength (subset),

Profiles dependent on the longitudinal coordinate use (x), and corresponding zone-wise values (used where applicable) carry subscript i . Zone-wise stiffness variables of models were omitted for readability. FB = flat-wise bending; DE = dynamic excitation; FE = finite element; CM = meshless continuum model

was applied at specimen level: for each indicator, regression models were fitted on $n - 1$ specimens and used to predict the omitted specimen, yielding a set of out-of-sample prediction errors. MAE and RMSE are computed from these pooled LOO errors, while in-sample R^2 is reported for descriptive reference only. The cross-validated coefficient of determination R_{LOO}^2 is computed from the LOO predictions relative to the mean-strength baseline; negative values indicate no predictive power beyond the sample mean.

3 Results and discussion

Selected results are presented in the following subsections; the complete dataset, including all raw and processed values, is published separately (Huber et al. 2025). Of the 56 specimens, three (IDs 25, 42, 44) were excluded from comparisons across bending tests, dynamic excitation, and CT-based models. All three exhibited substantially damaged ends, resulting in inconsistent effective lengths between CT scanning and mechanical testing. Because the final trimming of the broken ends prior to bending tests could not be reconstructed, these specimens lacked a reliable longitudinal reference.

Two of the excluded specimens had been tested to failure, reducing the number of valid bending strength results to 13 and the subset with measured MC_{FB} to 26. No exclusions were made for the visual grading analysis.

For three additional specimens (IDs 7, 27, 38), FE mesh generation failed due to extensive cavities from nail

extraction, and FE-based indicating properties could not be obtained for these cases.

3.1 Reference measurements and consistency

Selected distributions of moisture content, density, bending stiffness, and bending strength are summarised in Fig. 7a–d. These values serve as reference measurements against which the different indicators are compared. Complete raw and processed data are provided separately (Huber et al. 2025).

MC differed between measurement stages. Values obtained shortly after arrival in Tallinn for the dynamic-excitation tests, MC_{DE} , showed a broad spread, likely reflecting varying exposure during transport in rainy weather and interim storage. Gravimetric values MC_{FB} , obtained after several weeks of laboratory conditioning for a subset of specimens, were lower and less variable, consistent with indoor conditions. No direct MC measurements were available during CT scanning; based on storage records, specimens were expected to be comparatively dry at that stage. Consequently, differences in MC between measurement stages contribute to systematic offsets among density- and stiffness-related quantities derived from different methods.

Density estimates derived after the bending test and from the dynamic-excitation data show similar central tendencies (Fig. 7b). The lower mean of ρ_{CT} is consistent with the lower expected MC during CT acquisition. As MC correction affected density distributions only marginally and was unavailable for all specimens, unadjusted ρ_{FB} was retained for better comparative analyses.

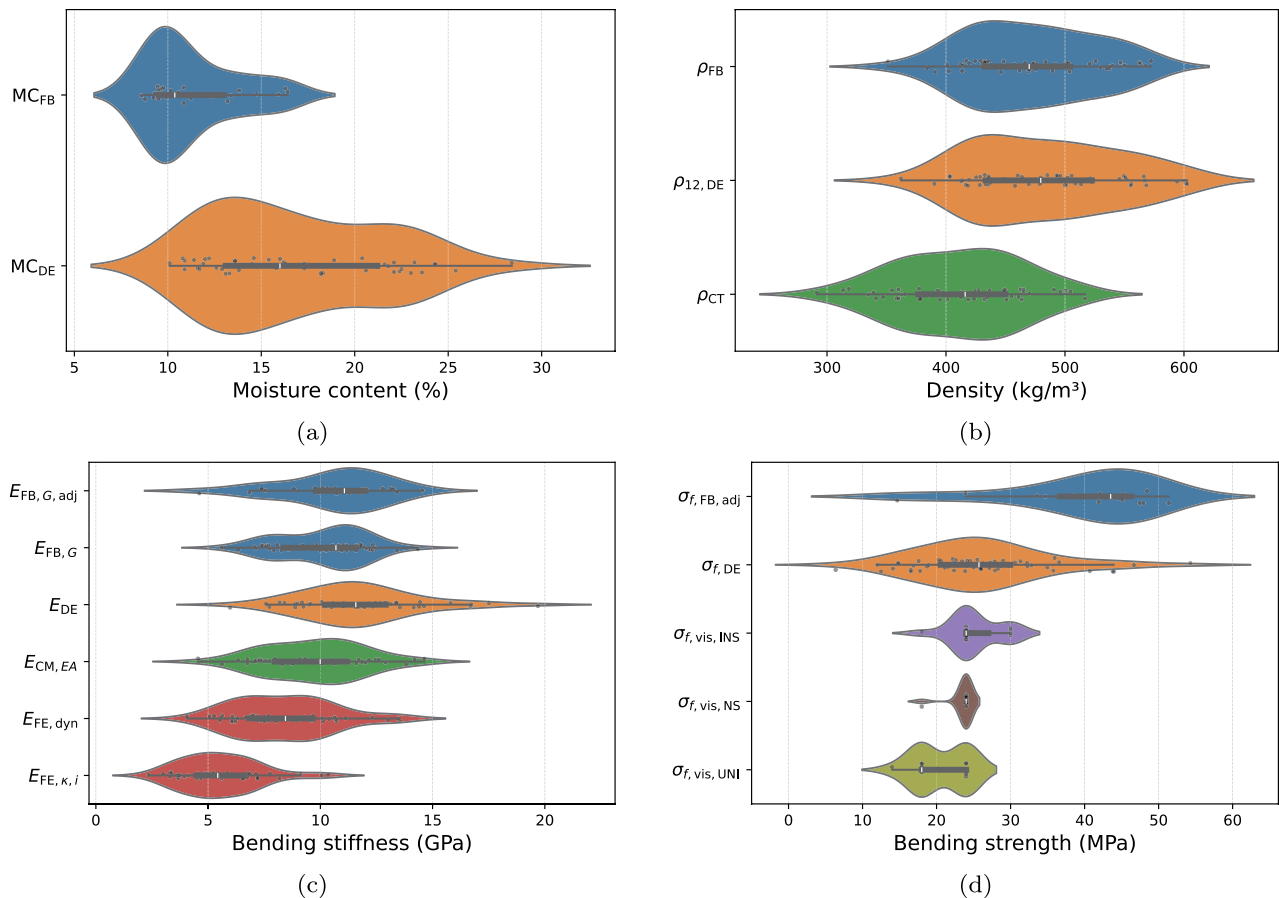


Fig. 7 Distributions of key properties across measurement and evaluation modalities: **a** moisture content, **b** density, **c** bending stiffness, and **d** bending strength



Fig. 8 Failure initiation in the proximity of a knot at the bottom surface during flat-wise bending

Stiffness values from flatwise tests, dynamic excitation, and CT-derived indicators exhibit comparable spreads but differ in central tendency (Fig. 7c). Dynamic-excitation stiffness tends to exceed bending-test values, consistent with the known influence of dynamic loading and density assumptions. CT-derived stiffness indicators show similar variability but a lower mean, reflecting both MC differences

during scanning and modelling assumptions. These systematic shifts are therefore interpreted as methodological offsets rather than material differences.

Bending strength values, available for 13 specimens, show substantially greater scatter across estimation methods (Fig. 7d). Visual grading yields narrow, conservative ranges, while dynamic-excitation based estimates span a wider interval centred near the nominal C24 level. Owing to the limited number of destructive tests, strength values are used primarily as contextual reference and for exploratory comparison of indicators.

Failure in destructive tests occurred predominantly near knots and regions of pronounced fibre deviation (Fig. 8). Corresponding FE stress analyses showed elevated transverse stress magnitudes in these regions (Fig. 9), indicating consistency between observed failure locations and modelled stress concentrations. This agreement supports the use of CT-derived structural information for identifying mechanically relevant features, even where absolute strength prediction remains uncertain.

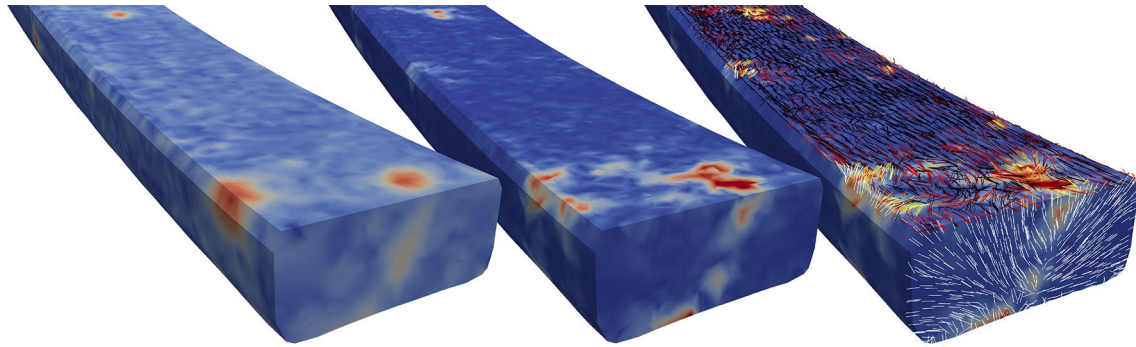


Fig. 9 FE model of Specimen 1 in bent configuration: density (left), transverse stress $\sqrt{\sigma_x^2 + \sigma_t^2}$ (middle), and overlay plot of longitudinal material orientation on top surface and radial orientation in cross section (right). Colour scale from blue (low) to red (high)

3.2 Comparative performance of indicators

3.2.1 Visual assessment

Figure 10 relates visual grading outcomes to experimentally determined properties. Most specimens fell into a single grade (NS 3691) or the highest two categories of the other applied standards, resulting in limited discriminatory resolution. This reflects the comparatively homogeneous origin and initial grading of the material as well as the known tendency of visual grading to prioritise conservative classification.

Across the evaluated properties, visual grades show only weak and inconsistent trends. Slight monotonic increases with grade are observable for bending stiffness and strength, but with substantial overlap between categories. Corresponding Spearman rank correlations (Fig. 11) remain low, confirming the limited predictive power of visual grading for this reclaimed stock.

This outcome is consistent with previous studies on reused structural timber, which report that visual criteria alone rarely capture the mechanical variability introduced by prior use, local damage, or internal features (Ranttila et al. 2025; Godina et al. 2025). In the present dataset, where most elements already satisfied relatively high visual quality thresholds, visual grading primarily serves as a coarse screening tool rather than a quantitative predictor of mechanical performance.

3.2.2 Zone-wise stiffness profiles

Zone-wise bending tests provided spatially resolved reference stiffness values against which CT-derived indicators could be compared. Representative profiles for selected specimens are shown in Figs. 12, 13, 14, 15, 16. Complete results for all specimens are included in the published dataset (Huber et al. 2025).

Both CM- and FE-based stiffness profiles reproduce the principal spatial trends observed in the experimental measurements. Local reductions in experimental stiffness coincide with knots and regions of fibre deviation visible in the density projections, indicating that the orientation and density information extracted from CT data captures mechanically relevant structural features. Knots emerging on the flat face produced more pronounced reductions in flatwise bending stiffness than knots located on side faces, consistent with the applied bending orientation.

Differences between modelling approaches are primarily related to smoothing and scaling. CM-based profiles respond more locally to density and orientation gradients, while FE-based profiles are smoother due to filtering and meshing steps. Localised high-density inclusions, for example remnants of fasteners, can generate gradient fields that are interpreted as fibre disturbances, producing local stiffness reductions. Such effects remain spatially confined in CM-based profiles but extend over larger regions in the FE-based representations.

Despite these differences in magnitude, the spatial correspondence between measured and model-derived stiffness variations remains robust across specimens with distinct defect patterns and density features. The results demonstrate that CT-derived structural indicators can reproduce relative intra-specimen stiffness variations even when absolute stiffness levels differ due to moisture-state or modelling assumptions (Fig. 17).

3.2.3 Specimen- and zone-level comparisons

Regression heatmaps (Figs. 18, 19, 20, 21, 22, 23) summarise the relationships between predictors and experimentally determined stiffness at both zone and specimen level. Bending strength is excluded from these general heatmaps due to the limited number of destructive tests and is instead evaluated separately using LOO cross-validation (Fig. 24).

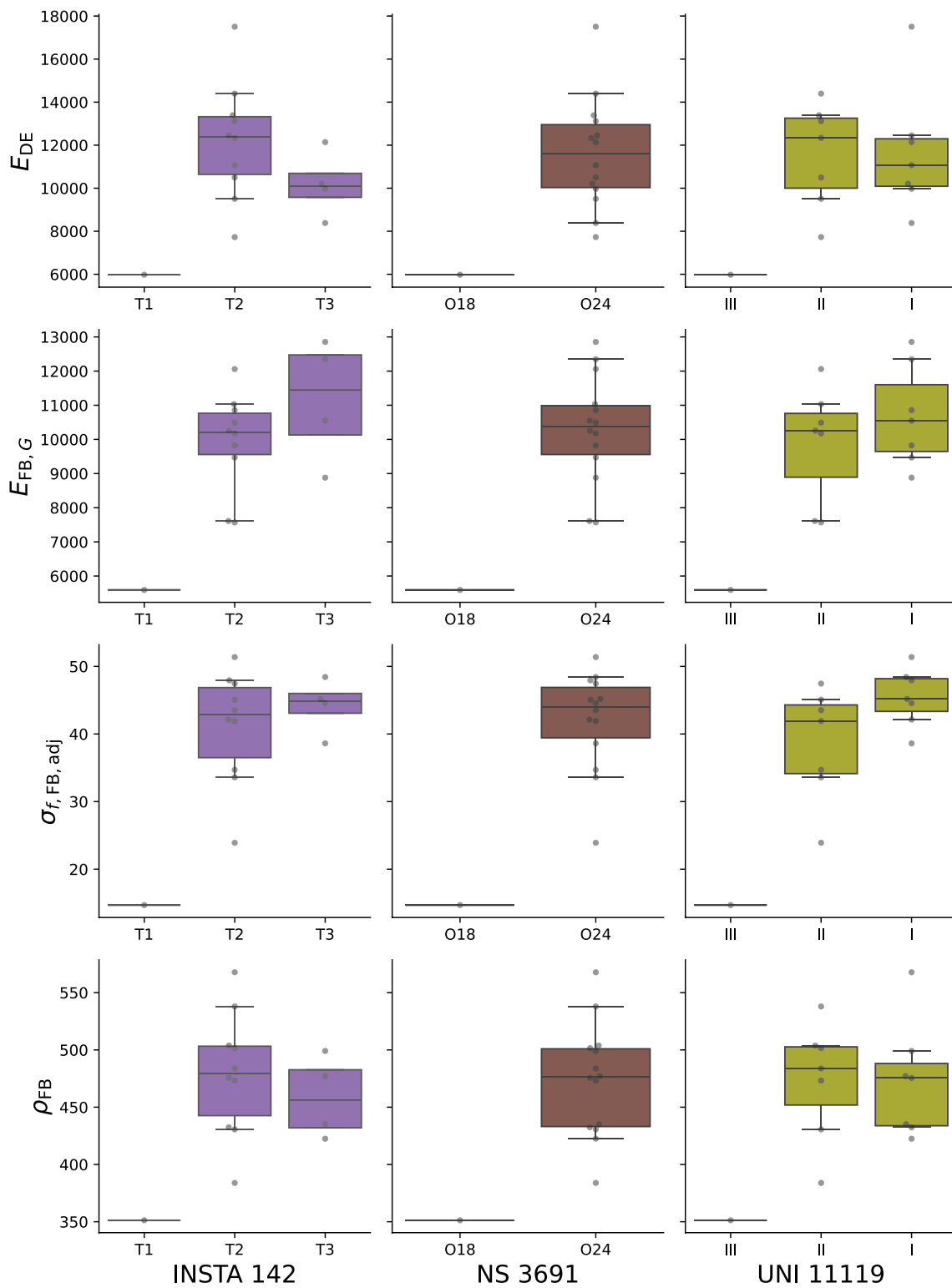


Fig. 10 Distributions of experimentally measured mechanical properties across visual grading categories from the applied standards

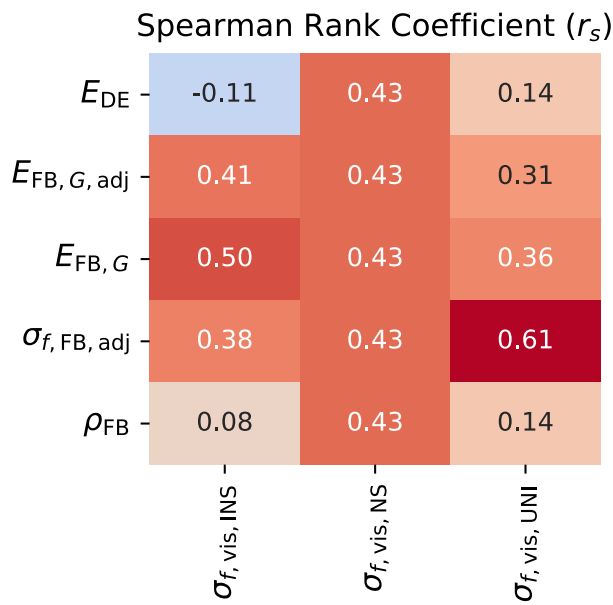


Fig. 11 Spearman rank correlation coefficients (r_s) between visual grading categories and experimentally measured values. Higher absolute values indicate stronger monotonic association

At zone level, R^2 values remain modest and errors comparatively high for all predictors. This reflects both the limited locality of the bending test reference values, since global-spans measurements with shear influence had to be used, and the model inaccuracies, such as unknown moisture state or sensitivity to spurious density gradients. Nevertheless, CT-derived CM and FE indicators consistently

outperform density alone, indicating that structural information contained in density gradients and inferred fibre orientation enhances predictive capability beyond bulk density.

At specimen level, predictive performance improved. Dynamic excitation provided the strongest single predictor of global bending stiffness. Its performance here is only slightly lower to that reported for new timber (Hanhijärvi and Ranta-Maunus 2008), which could be due to the relatively short length of some of the specimens (Ranttila et al. 2025) and the flatwise orientation.

Among CT-derived indicators, the CM-based stiffness measures $E_{CM,EA}$ and $E_{CM,EI}$ show the best predictive capability for experimental stiffness, again outperforming ρ_{CT} alone. This confirms that incorporating orientation-related information from volumetric density fields provides additional explanatory power. FE-based indicators show weaker correlations overall, except for the frequency-derived $E_{FE,dyn}$, which retains partial predictive value despite systematic underestimation of stiffness noted earlier.

Strength-related comparisons (Fig. 24) remain exploratory due to the limited number of destructive tests, but the LOO results are informative for relative ranking of indicators. For the strongest predictors (dynamic-excitation stiffness and the CM-based stiffness indicators), in-sample R^2 and cross-validated R^2_{LOO} differ considerably less than for other indicators, suggesting that their association with strength is not driven by single influential specimens. In contrast, several weaker indicators show large deviations and even negative R^2_{LOO} , indicating no predictive power

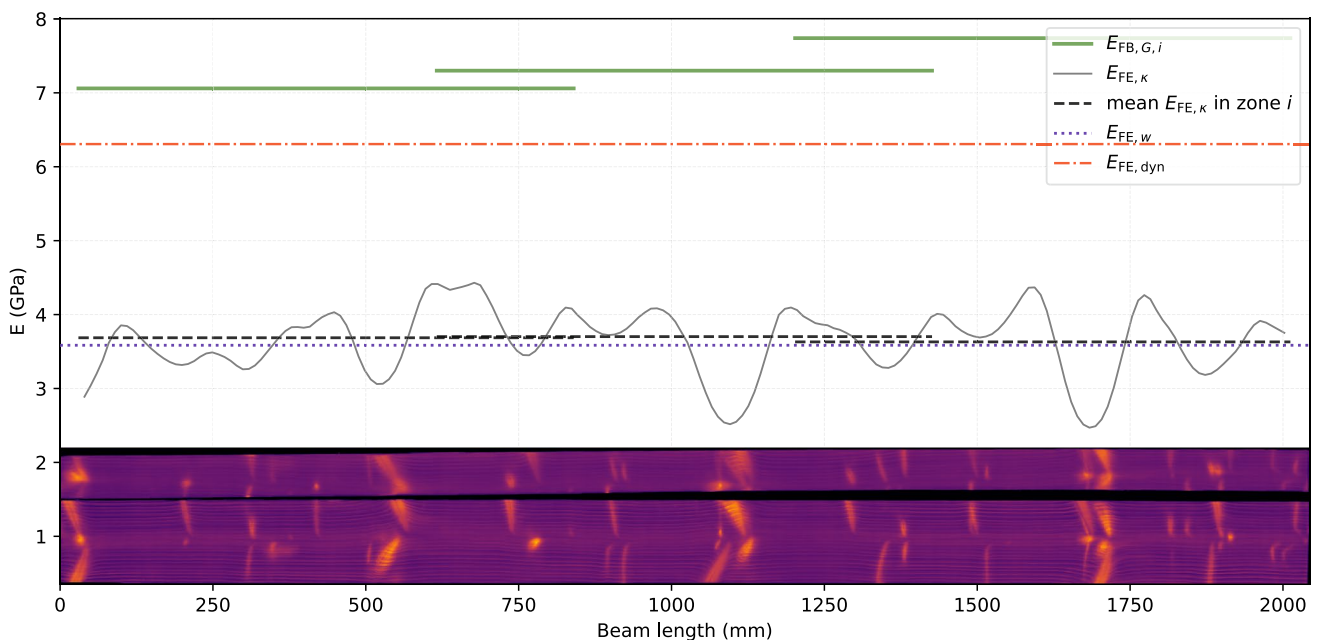


Fig. 12 Specimen 1: experimental zone-wise stiffness $E_{FB,G,i}$ compared with the FE stiffness profile $E_{FE,\kappa}(x)$, its zone averages, and global FE estimates $E_{FE,w}$ and $E_{FE,dyn}$. Density projection averages along the strong and weak axes are shown below

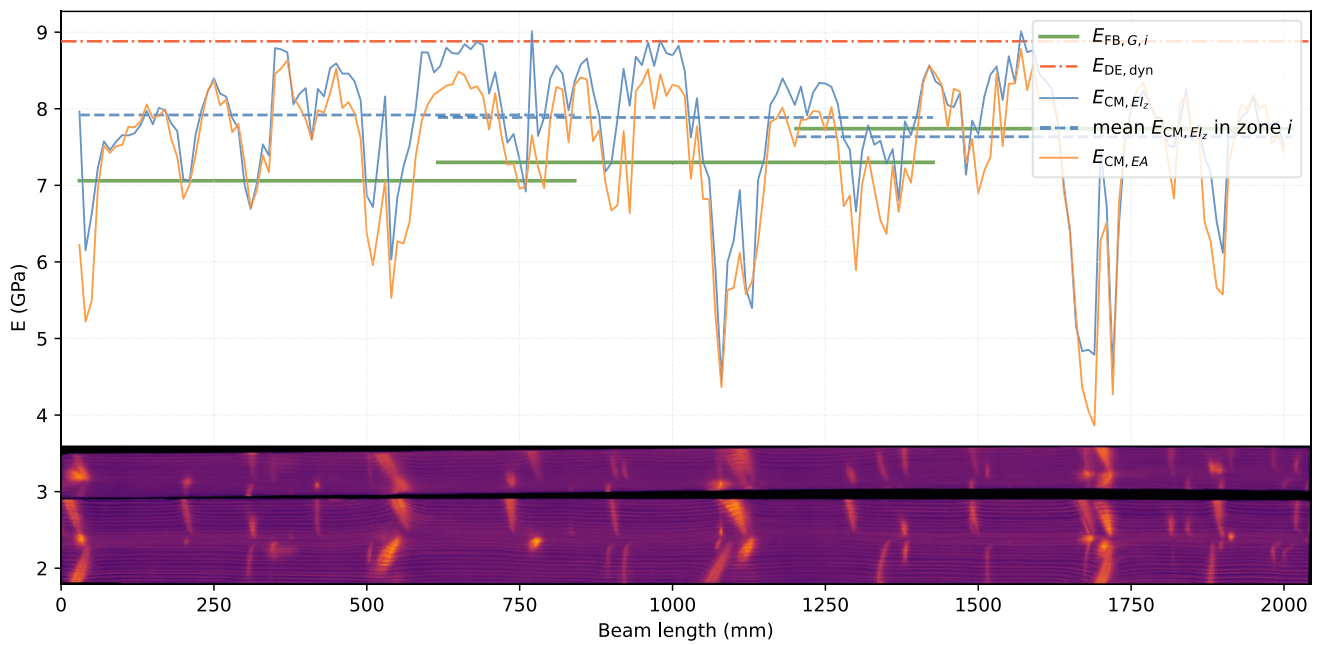


Fig. 13 Specimen 1: experimental zone-wise stiffness $E_{FB,G,i}$ compared with meshless model profiles $E_{CM,El_z}(x)$ and $E_{CM,EA}(x)$, including zone averages. Density projection averages along the strong and weak axes are shown below

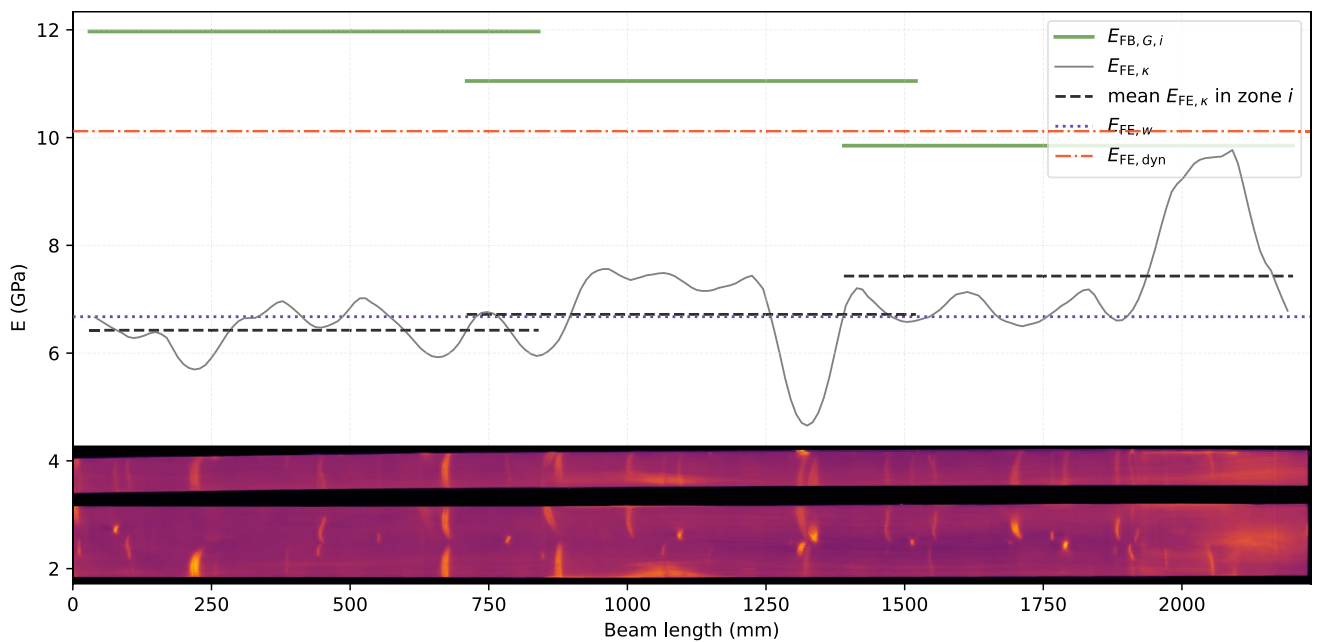


Fig. 14 Specimen 6: experimental zone-wise stiffness $E_{FB,G,i}$ compared with the FE stiffness profile $E_{FE,\kappa}(x)$, its zone averages, and global FE estimates $E_{FE,w}$ and $E_{FE,dyn}$. Density projection averages along the strong and weak axes are shown below

beyond the mean-strength baseline under the present conditions.

For context, the predictive performance observed here lies within the range reported for reclaimed softwood in recent studies. For recovered Norway spruce, longitudinal vibration indicators have been reported to predict global bending stiffness and strength with coefficients of determination on the order of $R^2 \approx 0.7-0.8$ (Llana et al. 2023). Comparable

reclaimed-timber datasets also show that vibration-based predictors generally outperform density-only or visual indicators for global stiffness estimation, while strength prediction remains substantially more uncertain (Niederwestberg et al. 2025; Ranttila et al. 2025).

The R^2 values obtained in the present study for dynamic excitation and for the strongest CT-derived stiffness

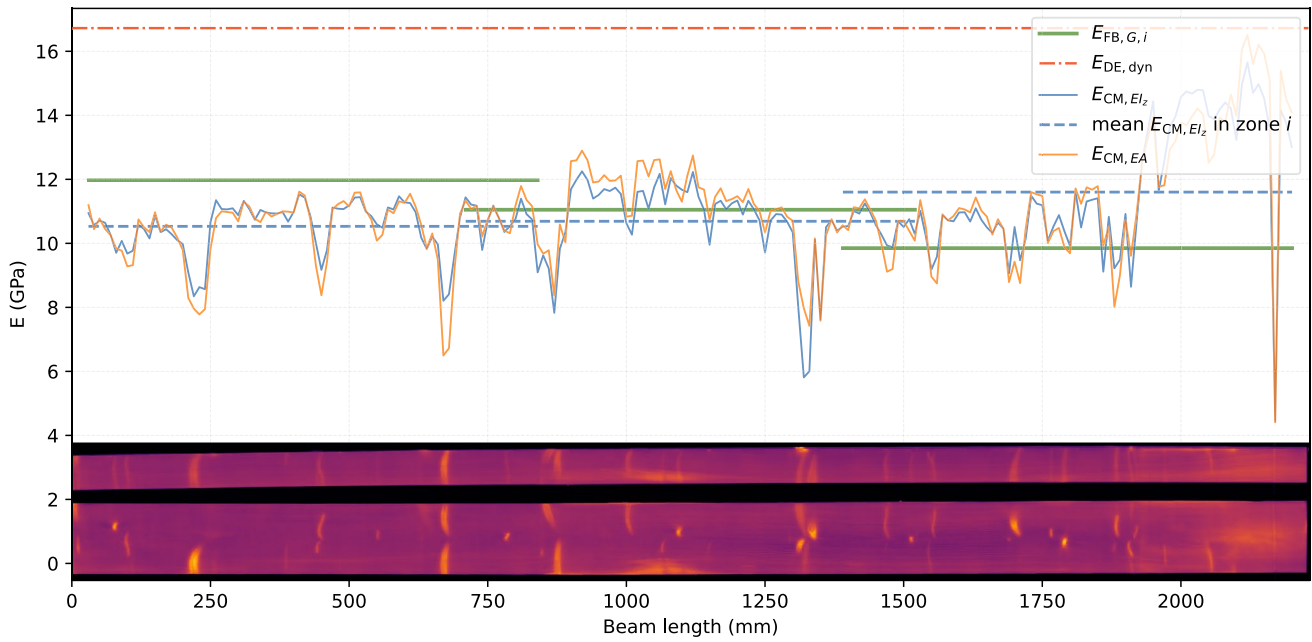


Fig. 15 Specimen 6: experimental zone-wise stiffness $E_{FB,G,i}$ compared with meshless model profiles $E_{CM,El_z}(x)$ and $E_{CM,EA}(x)$, including zone averages. Density projection averages along the strong and weak axes are shown below

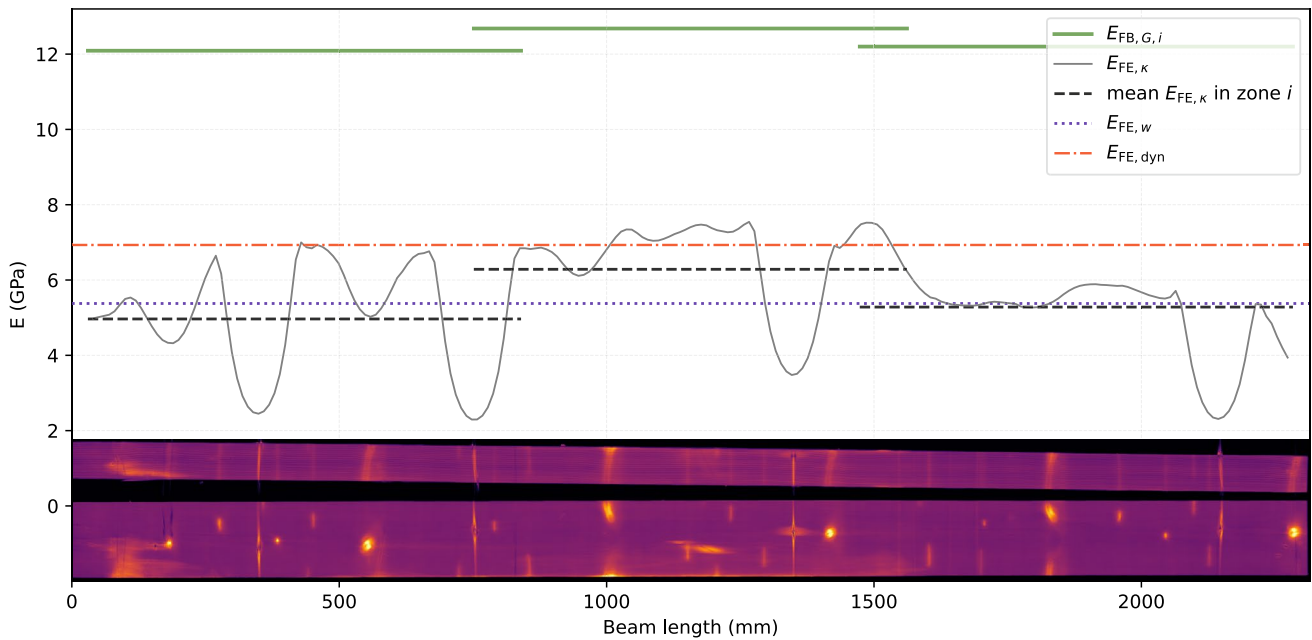


Fig. 16 Specimen 49: experimental zone-wise stiffness $E_{FB,G,i}$ compared with the FE stiffness profile $E_{FE,\kappa}(x)$, its zone averages, and global FE estimates $E_{FE,w}$ and $E_{FE,dyn}$. Density projection averages along the strong and weak axes are shown below

indicators therefore fall within the range expected for reclaimed structural softwood. Differences in absolute performance between studies can be attributed primarily to specimen geometry, test orientation, and moisture-state uncertainty, all of which are known to influence regression-based comparisons between non-destructive indicators and bending-test reference values.

The comparative results indicate that global stiffness can be captured reliably by established non-destructive methods such as dynamic excitation, while CT-derived indicators provide additional spatially resolved information on intra-specimen variability. Their principal contribution in the present context lies in resolving structural heterogeneity and enabling comparison of local stiffness patterns rather than in improving global strength prediction.

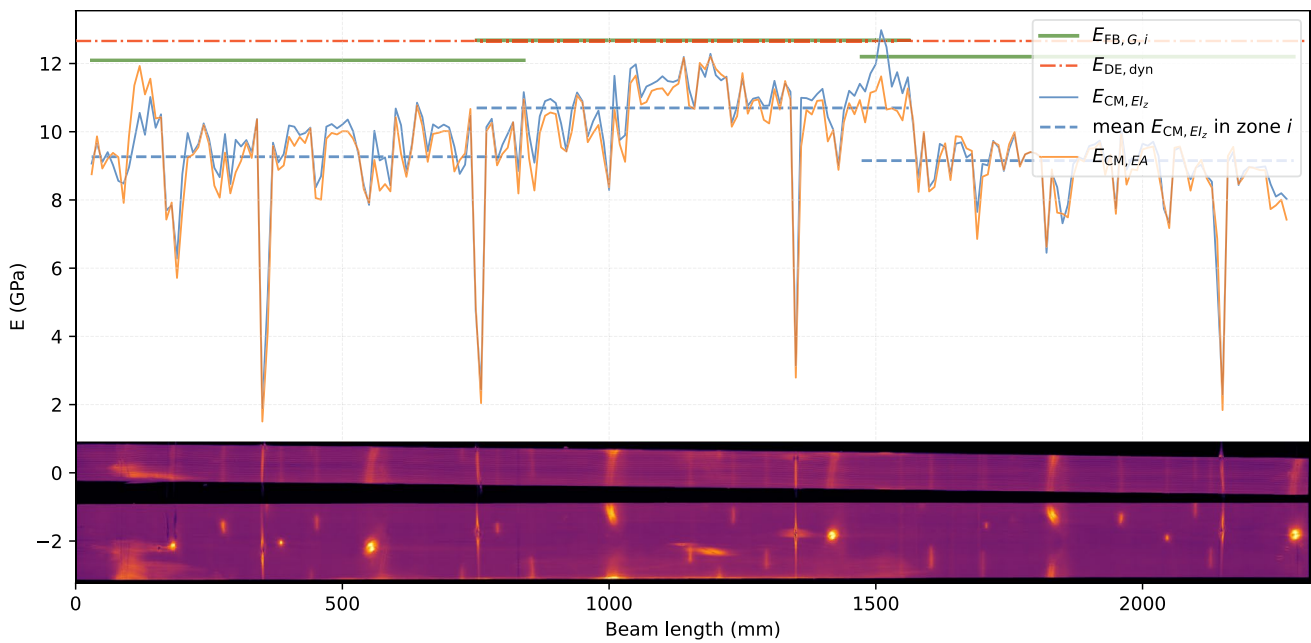


Fig. 17 Specimen 49: experimental zone-wise stiffness $E_{FB,G,i}$ compared with meshless model profiles $E_{CM,EI_z}(x)$ and $E_{CM,EA}(x)$, including zone averages. Density projection averages along the strong and weak axes are shown below

$E_{FB,G,adj}$	1.00	0.98	0.98	0.36	0.17	0.30	0.29	0.24	0.25
$E_{FB,G}$	0.98	1.00	1.00	0.25	0.16	0.26	0.24	0.19	0.18
E_{FB,G_w}	0.98	1.00	1.00	0.25	0.16	0.25	0.24	0.19	0.17
ρ_{FB}	0.36	0.25	0.25	1.00	0.69	0.81	0.79	0.82	0.90
	$E_{FB,G,adj}$	$E_{FB,G}$	E_{FB,G_w}	ρ_{FB}	$E_{FE,k,i}$	$E_{CM,EA,i}$	$E_{CM,EI,i}$	$G_{y,CM,GA,i}$	$\rho_{CT,i}$

Fig. 18 Zone-level coefficients of determination (R^2) for linear regressions between predictors (columns) and target variables (rows). Higher values indicate stronger explanatory power

$E_{FB,G,adj}$	1.00	0.99	0.99	0.60	0.41	0.54	0.53	0.49	0.50
$E_{FB,G}$	0.99	1.00	1.00	0.50	0.41	0.51	0.49	0.44	0.42
E_{FB,G_w}	0.99	1.00	1.00	0.50	0.40	0.50	0.49	0.44	0.42
ρ_{FB}	0.60	0.50	0.50	1.00	0.83	0.90	0.89	0.91	0.95
	$E_{FB,G,adj}$	$E_{FB,G}$	E_{FB,G_w}	ρ_{FB}	$E_{FE,k,i}$	$E_{CM,EA,i}$	$E_{CM,EI,i}$	$G_{y,CM,GA,i}$	$\rho_{CT,i}$

Fig. 20 Zone-level Pearson correlation coefficients (r) between predictors (columns) and target variables (rows). Higher absolute values indicate stronger linear association

$E_{FB,G,adj}$	0	320	327	1958	2008	1921	1936	2002	1987
$E_{FB,G}$	248	0	49	1771	1824	1732	1748	1804	1825
E_{FB,G_w}	210	41	0	1474	1514	1439	1452	1498	1515
ρ_{FB}	42	46	46	0	29	23	24	22	16
	$E_{FB,G,adj}$	$E_{FB,G}$	E_{FB,G_w}	ρ_{FB}	$E_{FE,k,i}$	$E_{CM,EA,i}$	$E_{CM,EI,i}$	$G_{y,CM,GA,i}$	$\rho_{CT,i}$

Fig. 19 Zone-level root-mean-square errors (RMSE) from linear regressions between predictors (columns) and target variables (rows). Lower values indicate higher predictive accuracy

To contextualise these trends, pairgrid visualisations are provided in the Supplementary Information (Online Resource 1), summarising all pairwise relationships among experimental variables and model-based indicators. They serve as a compact qualitative complement to the heatmap comparisons.

3.3 Methodological limitations

The present study evaluates a defined set of reclaimed elements of single species, cross-section, and initial grading. This controlled material stream enables consistent comparison of indicators but limits generalisation to more heterogeneous reclaimed timber populations. In particular, the restricted number of destructive tests precludes statistically

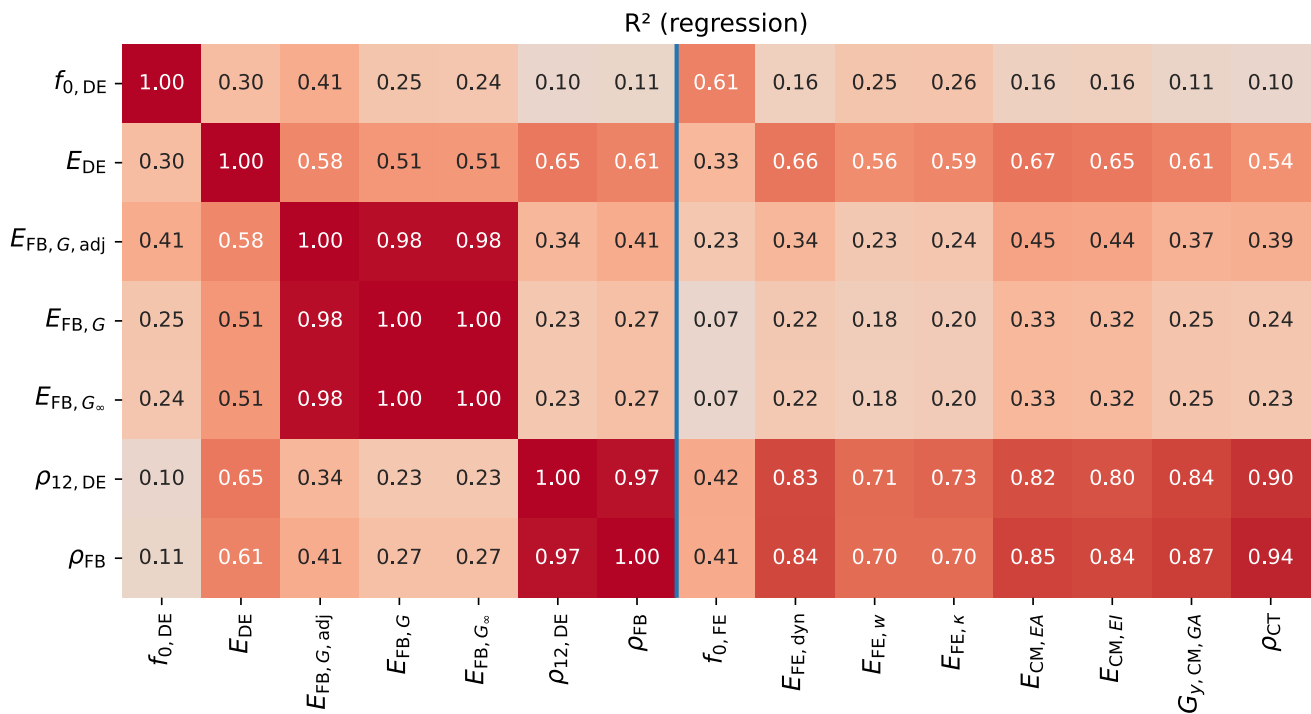


Fig. 21 Specimen-level coefficients of determination (R^2) from linear regressions between predictors (columns) and target variables (rows). Higher values indicate stronger explanatory power

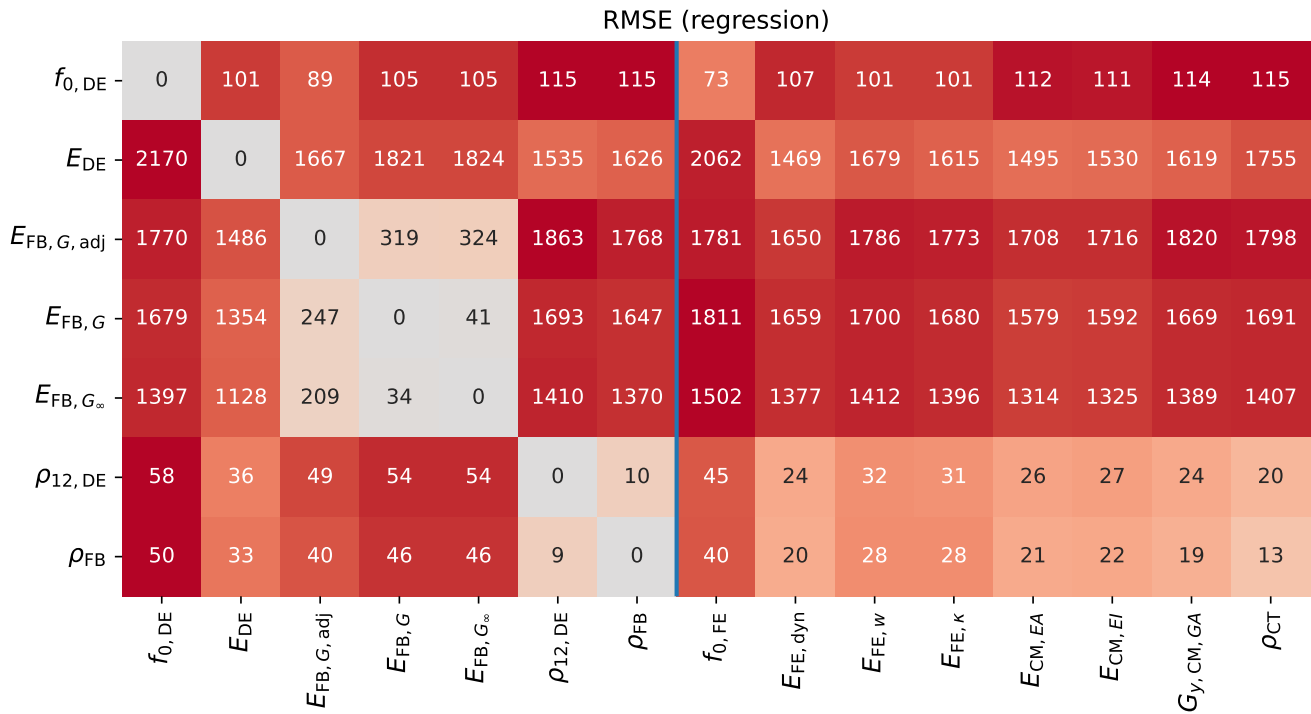


Fig. 22 Specimen-level root-mean-square errors (RMSE) from linear regressions between predictors (columns) and target variables (rows). Lower values indicate higher predictive accuracy

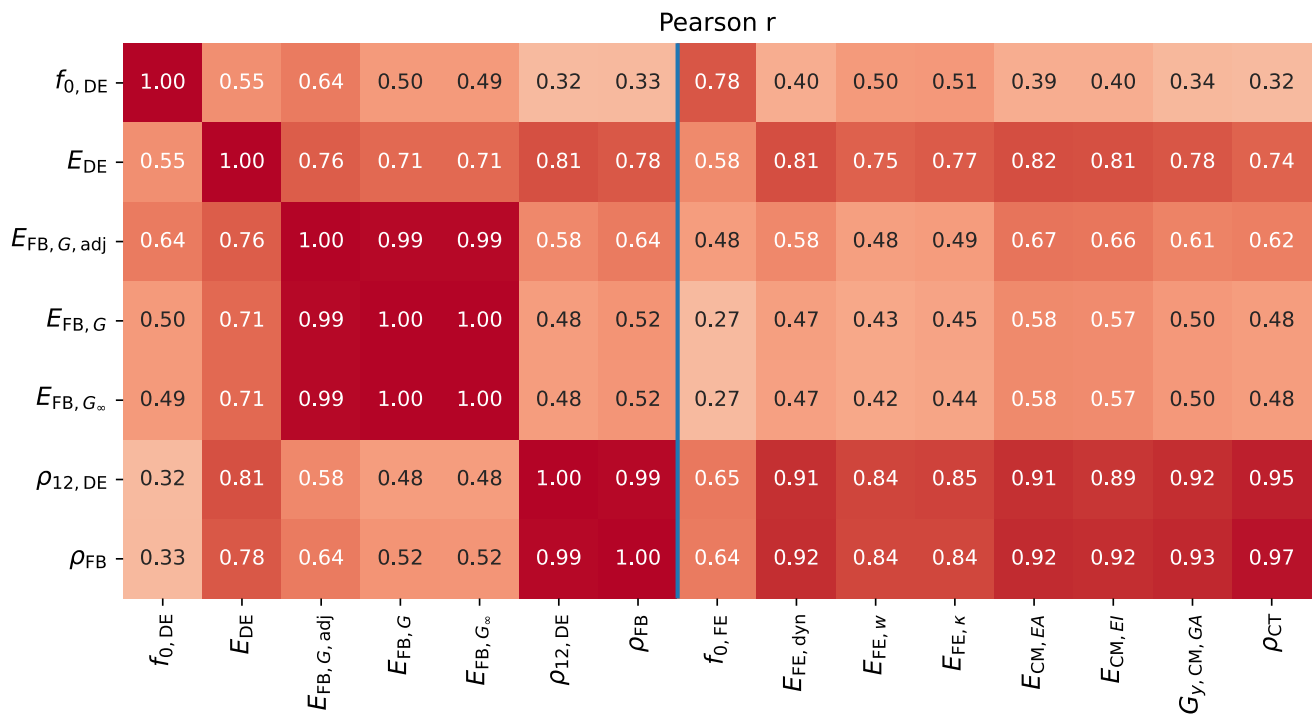


Fig. 23 Specimen-level Pearson correlation coefficients (r) between predictors (columns) and target variables (rows). Higher absolute values indicate stronger linear association

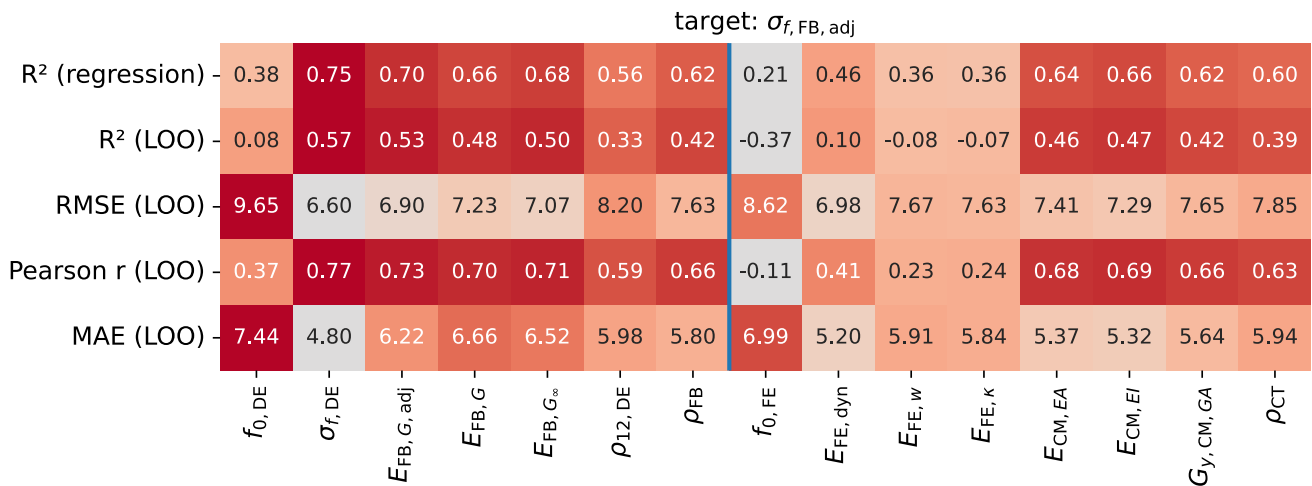


Fig. 24 Leave-one-out cross-validated (LOO) performance metrics for predicting $\sigma_{f,FB,adj}$ from the investigated indicators (columns). In-sample R^2 reported for descriptive reference

robust conclusions on bending strength and confines strength-related results to exploratory comparison.

Flatwise bending was selected to enable repeated zone-wise measurements and to align with the intended use of the material as lamellas in engineered products. However, most structural applications and strength-class definitions refer to edgewise behaviour. Differences between flatwise and edgewise stiffness and strength, arising from anisotropy, defect distribution through thickness, and shear effects, introduce additional uncertainty when relating the present results to

conventional grading frameworks. The reported stiffness values should therefore be interpreted primarily as comparative indicators within the tested configuration rather than as direct predictors of standard edgewise performance.

CT-derived indicators depend on calibration stability, segmentation thresholds, and gradient-based inference of fibre orientation. Cavities, metallic inclusions, and local density anomalies may distort these gradients and propagate into CM- and FE-based stiffness estimates. The FE discretisation was based on a sequence of processing and meshing

steps that may accumulate geometric deviations, including the smoothing of sharp edges and approximation of local surface irregularities. Mesh generation failed for specimens with severe internal cavities, introducing a bias toward less-degraded material. The curvature-based FE stiffness $E_{FE,\kappa}$ relied on numerical differentiation of displacement fields and appears in the denominator of the flexural formulation, making it intrinsically sensitive to noise.

Aggregation of high-resolution CT-derived profiles to zone or specimen level was performed using simple averaging to maintain consistency across methods. Alternative aggregation strategies or multi-modal predictors incorporating explicit defect descriptors may further improve predictive performance but were beyond the scope of the present comparative assessment. Together, these factors define the methodological boundaries within which the reported comparisons should be interpreted.

4 Conclusion

This study presents a comparative assessment of visual, dynamic, mechanical, and CT-derived indicators for piecewise evaluation of reclaimed Norway spruce timber from a controlled material stream. The objective was to examine how different indicators relate to experimentally measured stiffness and strength at both specimen and intra-specimen scale.

Dynamic excitation provided the most reliable single predictor of global bending stiffness. Visual grading showed limited discriminatory capability for this comparatively homogeneous stock. CT-derived indicators, particularly those incorporating orientation information from volumetric density fields, exceeded the predictive capability of density alone and reproduced the principal spatial stiffness variations observed in zone-wise bending tests. Their main contribution in the present context lies in resolving intra-specimen heterogeneity and providing structurally interpretable indicators.

Strength-related results are based on a small destructive subset and are therefore interpreted as indicative comparisons rather than statistically robust estimates. Leave-one-out evaluation indicates that the strongest stiffness-based indicators (dynamic excitation and CM-derived stiffness measures) retain comparable out-of-sample performance, whereas several weaker indicators collapse under cross-validation.

The results highlight that global stiffness can be assessed by the used non-destructive methods, while CT-based approaches provide complementary spatial information that may support allocation and optimisation in engineered wood products.

The study was restricted to a single species, cross-section, and initial strength class, and to flatwise bending relevant to reuse as a glulam lamella. Within these bounds, the results demonstrate the value of combining conventional and volumetric indicators to characterise reclaimed elements at specimen and sub-specimen scale.

Further work should evaluate the proposed comparative pipeline on more heterogeneous reclaimed timber populations and incorporate additional structural descriptors derived from CT data, such as knots, cavities, and fastener remnants. Expanded datasets with spatially resolved mechanical reference measurements will be required to assess robustness and to quantify uncertainty across material streams and reuse scenarios.

Supplementary Information The online version contains supplementary material available at <https://doi.org/10.1007/s00107-026-02433-1>.

Acknowledgements The research by Martin Tamke, Tom Svilans and Mette Ramsgaard Thomsen, as well as the material procurement and shipment, was conducted within the Ecometabolic Architecture project at CITA, funded by the European Research Council (ERC) under the European Union's Horizon 2020 research and innovation programme (grant agreement No. 101019693). Johannes Huber gratefully acknowledges support from His Majesty King Carl XVI Gustaf's 50th Anniversary Fund for Science, Technology, and Environment, the CT WOOD research programme at LTU Skellefteå and the European Union in the EIC Pathfinder Project "RAW: Computation For A New Age Of Resource Aware Architecture: Waste-Sourced And Fast-Growing Bio-Based Materials" (Project 101161441). The experimental work by Maarja Kauniste, Eero Tuhkanen and Alar Just was co-funded by the European Union and the Estonian Research Council via project TEM-TA80. The contribution by Wendy Wuyts was co-funded by the European Commission under the DRASTIC project (grant agreement No. 101123330). The timber elements were supplied by Omtre AS; we thank Christine Jørgensen and Ivar Ragnhildstveit for providing background information on the material supply.

Author contributions Johannes A. J. Huber conceived the overall study, defined the research direction, developed and implemented the CT-based modelling and analysis workflow, performed the CT data processing, numerical simulations, comparative evaluation, and full data curation, and led the writing of the original draft and manuscript revision. Tom Svilans contributed substantially to the conception and design of the study, co-developed the architecture and implementation of the CT-based modelling workflow, significantly contributed to methodological development and software implementation, and contributed to writing the original draft, data interpretation and manuscript revision. Maarja Kauniste performed the mechanical bending tests, contributed to data curation and validation, and supported the interpretation of experimental results and contributed to manuscript editing. Niels H. Vonk performed the dynamic excitation measurements, contributed to data curation and interpretation, and contributed to writing the original draft and manuscript revision. Olof Broman conducted the CT scanning and data acquisition, and supported specimen preparation and logistics. Eero Tuhkanen co-designed and supervised the mechanical testing, assisted with laboratory work, contributed to data curation and validation, and participated in manuscript revision. Wendy Wuyts contributed to writing the original manuscript and coordinated material procurement through Omtre AS, provided contextual information

on the material stream, and contributed to manuscript revision. Alar Just supervised the mechanical testing programme, contributed to experimental design and interpretation, and participated in manuscript revision. Martin Tamke contributed to writing the original draft and manuscript editing and together with Mette Ramsgaard Thomsen acquired funding, provided project supervision and conceptual guidance, contributed to methodological framing, and participated in manuscript revision. All authors revised the manuscript for intellectual content, approved the final version for publication, and agree to be accountable for all aspects of the work.

Funding Open access funding provided by Lulea University of Technology.

Data availability All CT volumes, mechanical tests, dynamic excitation data, visual grading results, and CM and FE model outputs as well as statistical evaluations used in this study are openly available on Zenodo: J. A. J. Huber, T. Svilans, M. Kauniste, N. H. Vonk, O. Broman, E. Tuhkanen, W. Wuys, A. Just, M. Tamke, M. Ramsgaard Thomsen, Multimodal reclaimed timber dataset: X-ray ct volumes, visual grading, dynamic tests, mechanical tests, and finite element and continuum model results with density, fibre orientation and stiffness fields, 2025. doi: <https://doi.org/10.5281/zenodo.17682666>

Declarations

Conflict of interest The authors have no conflict of interest to declare.

Open Access This article is licensed under a Creative Commons Attribution 4.0 International License, which permits use, sharing, adaptation, distribution and reproduction in any medium or format, as long as you give appropriate credit to the original author(s) and the source, provide a link to the Creative Commons licence, and indicate if changes were made. The images or other third party material in this article are included in the article's Creative Commons licence, unless indicated otherwise in a credit line to the material. If material is not included in the article's Creative Commons licence and your intended use is not permitted by statutory regulation or exceeds the permitted use, you will need to obtain permission directly from the copyright holder. To view a copy of this licence, visit <http://creativecommons.org/licenses/by/4.0/>.

References

- Asa P, El Feghali C, Steixner C, Tahouni Y, Wagner HJ, Knippers J, Menges A (2024) Embraced wood: circular construction method for composite long-span beams from unprocessed reclaimed timber, fibers and clay. *Constr Build Mater* 416:135096. <https://doi.org/10.1016/j.conbuildmat.2024.135096>
- Bergsagel D, Heisel F (2023) Structural design using reclaimed wood: a case study and proposed design procedure. *J Clean Prod* 420:138316. <https://doi.org/10.1016/j.jclepro.2023.138316>
- Bigun J, Bigun T, Nilsson K (2004) Recognition by symmetry derivatives and the generalized structure tensor. *IEEE Trans Pattern Anal Mach Intell* 26:1590–1605. <https://doi.org/10.1109/TPAMI.2004.126>
- Byers BS, Raghu D, Olumo A, De Wolf C, Haas C (2024) From research to practice: a review on technologies for addressing the information gap for building material reuse in circular construction. *Sustain Prod Consump* 45:177–191. <https://doi.org/10.1016/j.spc.2023.12.017>
- Cavalli A, Cibecchini D, Togni M, Sousa HS (2016) A review on the mechanical properties of aged wood and salvaged timber. *Constr Build Mater* 114:681–687
- Chúláin CU, Llana DF, Hogan P, McGetrick P, Harte AM (2023) Bending characteristics of clt from recovered spruce. In: *World Conference on Timber Engineering*, pp 888–894
- Churkina G, Organschi A, Reyer CPO, Ruff A, Vinke K, Liu Z, Reck BK, Graedel TE, Schellnhuber HJ (2020) Buildings as a global carbon sink. *Nature Sustain* 3:269–276. <https://doi.org/10.1038/s41893-019-0462-4>
- Crews K, MacKenzie C (2008). Development of grading rules for recycled timber used in structural applications, In: *World Conference on Timber Engineering*, WCTE
- Dhondt G (2004) The finite element method for three? Dimensional thermomechanical applications. 1 ed., Wiley. <https://doi.org/10.1002/0470021217>
- Dinwoodie JM (2000) *Timber: Its nature and behaviour*, 2nd edn. Taylor & Francis, New York, NY
- Dong W, Rose CM, Stegeman JA (2024a) Cross-laminated secondary timber: Validation of non-destructive assessment of structural properties by full-scale bending tests. *Eng Struct*, 298
- Dong W, Rose CM, Stegeman JA (2024) Cross-laminated secondary timber: validation of non-destructive assessment of structural properties by full-scale bending tests. *Eng Struct* 298:117029
- EN 1309–3, 2018. EN 1309–3: (2018) Round and sawn timber—methods of measurements—Part 3: Features and biological degradations. European Committee for Standardization (CEN): Brussels, Belgium
- EN 14081–1, 2019. EN 14081–1:2016+A1: (2019), Timber structures - Strength graded structural timber with rectangular cross section - Part 1: General requirements. European Committee for Standardization (CEN): Brussels, Belgium
- EN 14081–2, 2018. EN 14081–2: (2018) Timber structures - Strength graded structural timber with rectangular cross section - Part 2: Machine grading; additional requirements for type testing. European Committee for Standardization (CEN): Brussels, Belgium
- EN 1912, 2024. EN 1912: (2024) Structural Timber - Strength classes - Assignment of visual grades and species. European Committee for Standardization (CEN): Brussels, Belgium
- EN 338, 2016. EN 338: (2016) Structural timber - Strength classes. European Committee for Standardization (CEN): Brussels, Belgium
- EN 384, 2016. EN 384:(2016) Structural timber - Determination of characteristic values of mechanical properties and density. European Committee for Standardization (CEN): Brussels, Belgium
- EN 408, 2012. EN 408:2010+A1: (2012) - Timber structures - Structural timber and glued laminated timber - Determination of some physical and mechanical properties. European Committee for Standardization (CEN)
- Falk RH, Maul DG, Cramer SM, Evans J, Herian V (2008) Engineering properties of douglas-fir lumber reclaimed from deconstructed buildings. Research Paper FPL-RP-650. USDA Forest Service,
- Geuzaine C, Remacle JF (2009) Gmsh: A 3-D finite element mesh generator with built-in pre- and post-processing facilities. *Int J Numer Meth Eng* 79:1309–1331. <https://doi.org/10.1002/nme.2579>
- Godina M, Gowler P, Rose CM, Wiegand E, Mills HF, Koronaki A, Ramage MH, Shah DU (2025) Strategies for salvaging and repurposing timber elements from existing buildings in the UK. *J Clean Prod* 489:144629. <https://doi.org/10.1016/j.jclepro.2024.144629>
- Grüter C, Gordon M, Muster M, Kastner F, Grönquist P, Frangi A, Langenberg S, De Wolf C (2023) Design for and from disassembly with timber elements: strategies based on two case studies from Switzerland. *Front Built Environ*. <https://doi.org/10.3389/fbuil.2023.1307632>

- Haakonsen SM, Tomczak A, Izumi B, Luczkowski M (2024) Automation of circular design: a timber building case study. *Int J Archit Comput*. <https://doi.org/10.1177/14780771241234447>
- Hanhijärvi A, Ranta-Maunus A (2008) Development of strength grading of timber using combined measurement techniques: Report of the Combigrade-project - phase 2. VTT Technical Research Centre of Finland,(Technical Report)
- Hansson L, Couceiro J, Fjellner BA (2017) Estimation of shrinkage coefficients in radial and tangential directions from CT images. *Wood Mater Sci Eng* 12:251–256. <https://doi.org/10.1080/17480272.2016.1249405>
- Heisel F, Bergsagel D (2025) Structural reclaimed wood – reuse, re-use, and repurposing, In: Structures and Architecture. CRC Press. Num Pages: 8
- Howard M, Yan X, Mustafee N, Charnley F, Böhm S, Pascucci S (2022) Going beyond waste reduction: exploring tools and methods for circular economy adoption in small-medium enterprises. *Resour Conserv Recycl* 182:106345. <https://doi.org/10.1016/j.resconrec.2022.106345>
- Hu M, Olsson A, Abdeljaber O, Huber J (2025) Determining growth surfaces and fiber orientation in Norway spruce sawn timber using X-ray computed tomography and optical scanning. *Constr Build Mater* 482:141734. <https://doi.org/10.1016/j.conbuildmat.2025.141734>
- Hu M, Olsson A, Hall S, Seifert T (2022) Fibre directions at a branch-stem junction in Norway spruce: a microscale investigation using X-ray computed tomography. *Wood Sci Technol* 56:147–169. <https://doi.org/10.1007/s00226-021-01353-y>
- Hu MK (1962) Visual pattern recognition by moment invariants. *IEEE Trans Inf Theory* 8:179–187. <https://doi.org/10.1109/tit.1962.1057692>
- Huber J, Abdeljaber O, Oja J, Olsson A (2023) Evaluation of models of fibre orientation in sawn timber using synchronised computed tomography and optical scanning data. In: World conference on timber engineering (WCTE 2023), World Conference on Timber Engineering (WCTE 2023), Oslo, Norway. pp. 421–427. <https://doi.org/10.52202/069179-0057>
- Huber JA, Broman O, Ekevad M, Oja J, Hansson L (2022) A method for generating finite element models of wood boards from X-ray computed tomography scans. *Comput Struct* 260:106702. <https://doi.org/10.1016/j.compstruc.2021.106702>
- Huber JAJ (2021) Numerical modelling of timber building components to prevent disproportionate collapse. Phd thesis. Luleå University of Technology. <https://doi.org/10.5281/zenodo.15464980>
- Huber JAJ, Svilans T, Kauniste M, Vonk NH, Broman O, Tuhkanen E, Wuyts W, Just A, Tamke M, Ramsgaard Thomsen M (2025) Multimodal reclaimed timber dataset: X-ray ct volumes, visual grading, dynamic tests, mechanical tests, and finite element and continuum model results with density, fibre orientation and stiffness fields. <https://doi.org/10.5281/zenodo.17682667>
- Hudert M, Pfeiffer S (2019). Rethinking wood: future dimensions of timber assembly. In: Rethinking Wood. Birkhäuser. <https://doi.org/10.1515/9783035617061>
- Katsevich A (2004) An improved exact filtered backprojection algorithm for spiral computed tomography. *Adv Appl Math* 32:681–697. [https://doi.org/10.1016/S0196-8858\(03\)00099-X](https://doi.org/10.1016/S0196-8858(03)00099-X)
- Kauniste M, Just A, Tuhkanen E, Kalamees T (2024) Assessment on strength and stiffness properties of aged structural timber. *J Sustain Archit Civ Eng* 34:62–74. <https://doi.org/10.5755/j01.sace.34.1.35534>
- Krause M, Hausherr JM, Burgeth B, Herrmann C, Krenkel W (2010) Determination of the fibre orientation in composites using the structure tensor and local X-ray transform. *J Mater Sci* 45:888–896. <https://doi.org/10.1007/s10853-009-4016-4>
- Lebossé M, Halin G, Besancon F, Fuchs A (2022) Incorporating BIM Practices into Reuse Process of Timber - Propositions of a digital workflow and tool for reclaiming structural pieces of wood, in: eCAADe 2022: Co-creating the Future - Inclusion in and through Design. Ghent, France, pp 205–214. <https://doi.org/10.52842/conf.ecaade.2022.1.205>
- Lindgren O (1992) Medical CT-Scanners for Non-Destructive Wood Density and Moisture Content Measurements. Luleå University of Technology,(Ph.D. thesis)
- Llana DF, Íñiguez González G, Plos M, Turk G (2023) Grading of recovered norway spruce (picea abies) timber for structural purposes. *Constr Build Mater* 398:132440. <https://doi.org/10.1016/j.conbuildmat.2023.132440>
- Longuetaud F, Mothe F, Kerautret B, Krähenbühl A, Hory L, Leban J, Debled-Rennesson I (2012) Automatic knot detection and measurements from X-ray CT images of wood: A review and validation of an improved algorithm on softwood samples. *Comput Electron Agric* 85:77–89. <https://doi.org/10.1016/j.compag.2012.03.013>. (publisher: Elsevier B.V)
- Lorensen WE, Cline HE (1987) Marching cubes: a high resolution 3d surface construction algorithm. *ACM SIGGRAPH Comput Graph* 21:163–169. <https://doi.org/10.1145/37402.37422>
- Luengo C, Contributors D (2025) DIPLib: Quantitative Image Analysis in C++, MATLAB and Python. DIPLib Project. Version 3.x, <https://github.com/DIPLib/diplib>
- Lukacevic M, Kandler G, Hu M, Olsson A, Füssli J (2019) A 3D model for knots and related fiber deviations in sawn timber for prediction of mechanical properties of boards. *Mater Des* 166:107617. <https://doi.org/10.1016/j.matdes.2019.107617>
- Moltini G, Íñiguez González G, Cabrera G, Baño V (2022) Evaluation of yield improvements in machine vs. visual strength grading for softwood species. *Forests* 13:2021. <https://doi.org/10.3390/f13122021>
- Museth K (2013) Vdb: High-resolution sparse volumes with dynamic topology. *ACM Trans Graph*. <https://doi.org/10.1145/2487228.2487235>
- Niederwestberg J, Weijs HJJ, Vonk NH, Jong Jd (2025) Structural potential of reclaimed and local timber as new resources in The Netherlands, In: Structures and architecture. CRC Press. Num Pages: 8
- Novais Passarelli R, Chiletto TDO, Brandner R, Ottenhaus LM (2025) Circulation of structural timber for structural purposes: a review of opportunities and challenges. *Wood Mater Sci Eng* 20:778–799. <https://doi.org/10.1080/17480272.2025.2493711>
- NS 3691–3, 2025. NS 3691–3: (2025) - Evaluering av returtré - Del 3: Visuelt styrkesortering (Evaluation of reclaimed timber - Part 3: Visual strength grading). Standard Norge
- Nußholz J, Çetin S, Eberhardt L, De Wolf C, Bocken N (2023) From circular strategies to actions: 65 European circular building cases and their decarbonisation potential. *Resour Conserv Recycl Adv* 17:200130. <https://doi.org/10.1016/j.rcradv.2023.200130>
- Ormarsson S (1999) Numerical analysis of moisture-related distortions in sawn timber. Ph.D. thesis. Chalmers University of Technology. ISBN: 9171978348 ISSN: 0346718X
- Piazza M, Del Senno M (2021) Proposals and criteria for the preliminary evaluation, the design and the execution of works on ancient load bearing timber structures. *Wooden Handwork/Wooden Carpentry, European Restoration Sites*, pp 263–277
- Piazza M, Riggio M (2008) Visual strength-grading and NDT of timber in traditional structures. *J Build Apprais* 3:267–296. <https://doi.org/10.1057/jba.2008.4>
- Prewitt JMS, Mendelsohn ML (1966) The analysis of cell images. *Ann N Y Acad Sci* 128:1035–1053. <https://doi.org/10.1111/j.1749-6632.1965.tb11715.x>
- Pronk A, Brancart S, Sanders F (2022) Reusing timber formwork in building construction: testing, redesign, and socio-economic reflection. *Urban Plan* 7:81–96

- Rais A, Ursella E, Vicario E, Giudiceandrea F (2017) The use of the first industrial X-ray CT scanner increases the lumber recovery value: case study on visually strength-graded Douglas-fir timber. *Ann For Sci* 74:28. <https://doi.org/10.1007/s13595-017-0630-5>
- Ramsgaard Thomsen M, Nicholas P, Rossi G, Daugaard AE, Rech A (2023) Extending the circular design framework for bio-based materials. *Design for rethinking resources - UIA World Congress of Architectur 2023 (UIACPH2023)*, 609 Publisher: Springer Nature Swizerland AG
- Ranttila H, Fink G, Brandner R, Ridley-Ellis D (2025) Circulating structural timber and engineered wood products—challenges and potentials towards reliable evaluation of mechanical properties. *Wood Mater Sci Eng* 20:910–925. <https://doi.org/10.1080/17480272.2025.2517186>
- Ravenshorst G, van de Kuilen J (2013) Adjustment factor for moisture content for the wave speed measured with mtgbatch, escan and mtg. *tg1/0613/04rev. b*
- Ridley-Ellis D, Stapel P, Baño V (2016) Strength grading of sawn timber in Europe: an explanation for engineers and researchers. *Eur J Wood Wood Prod* 74:291–306. <https://doi.org/10.1007/s00107-016-1034-1>
- Rinn F, Schweingruber FH, Schär E (1996) Resistograph and x-ray density charts of wood. comparative evaluation of drill resistance profiles and x-ray density charts of different wood species. *Holzforchung* 50:303–311. <https://doi.org/10.1515/hfsg.1996.50.4.303>
- Rose CM, Bergsagel D, Dufresne T, Unubreme E, Lyu T, Duffour P, Stegemann JA (2018) Cross-laminated secondary timber: experimental testing and modelling the effect of defects and reduced feedstock properties. *Sustainability* 10:4118
- Savitzky A, Golay MJE (1964) Smoothing and differentiation of data by simplified least squares procedures. *Anal Chem* 36:1627–1639. <https://doi.org/10.1021/ac60214a047>
- SS 230120, 2010. SS 230120: (2010) Nordic visual strength grading rules for timber (INSTA 142). 2nd ed., Swedish Standards Institute (SIS): Stockholm, Sweden
- Svilans T, Tamke M, Ramsgaard Thomsen M (2022). Integrative strategies across the timber value chain. In: *Proceedings of the 5th international conference on structures and architecture (ICSA)*
- Tamke M, Gatz S, Svilans T, Ramsgaard Thomsen M (2021) Tree-to-Product: Prototypical workflow connecting Data from tree with fabrication of engineered wood structure - RawLam. In: *Proceedings of WCTE2021, Santiago, Chile*. pp 2754–2763
- UNI 11119, 2004. UNI 11119: (2004) Cultural heritage - Wooden artefacts - Load-bearing structures - On site inspections for the diagnosis of timber members. Ente Nazionale Italiano di Unificazione (UNI) Milan, Italy
- Vonk NH, Niederwestberg J, Oorschot RWA, de Jong JD (2024). Upcycling of single-use pallet wood to cross laminated timber. In: *Accepted for publication in the 1st international conference on net-zero built environment*
- Zhou QY, Park J, Koltun V (2018) Open3d: A modern library for 3d data processing. <https://doi.org/10.48550/ARXIV.1801.09847>

Publisher's Note Springer Nature remains neutral with regard to jurisdictional claims in published maps and institutional affiliations.